Isabella Diem BSc.

Solid state synthesis of fluoride garnets

Master's Thesis

to achieve the university degree of
Diplom-Ingenieurin
Master's degree programme: Advanced Materials Science

submitted to
Graz University of Technology

Supervisor:
Univ. -Prof. Dr. rer.nat. Martin Wilkening
Co-Supervisor:
Dr. techn. Daniel Rettenwander

Institute for Chemistry and Technology of Materials

Graz, June 2020

Affidavit

I declare that I have authored this thesis independently, that I have not used other than the declared sources/resources, and that I have explicitly indicated all material which has been quoted either literally or by content from the sources used. The text document uploaded to TUGRAZonline is identical to the present master‘s thesis.

Date: _____ Signation: _____

Acknowledgement

First of all, I would like to thank Prof. Martin Wilkening and Dr. Daniel Rettenwander for the possibility to do my thesis at the Institute for Chemistry and Technology of Materials. I also would like to thank Dr. Martin Philipp. The door of his office was always open whenever I ran into a trouble spot or had a question.

I would like to thank Prof. Franz-Andreas and Dr. Brigitte Bitschnau for the X-ray powder diffraction (XRD) measurements of my samples.

Finally, I want to say thanks to the whole working group for the nice working atmosphere and for their help and advice.

Abstract

With increasing use of renewable energies, devices for an intermediate storage of energy peaks are needed. The most promising energy storage devices are lithium-ion liquid-electrolyte batteries. However, they have several drawbacks, including expensive sealing agents, inherent hazards of fire and leakages, low energy and power density. All solid state batteries utilize solid state electrolytes to overcome these issues. Hence, active research on new materials to overcome current limitations of these technologies has to be made. During this work the solid state synthesis of Cryolithionite ($Na_3Al_2Li_3F_{12}$) which naturally occurs in Greenland is improved. A synthetically modified structure of these chemical composition has the potential to overcome current limitations by combining high Li-ion conductivity and a high electrochemical stability. This could have an high impact on the next generation of all solid state batteries (ASSBs). The preparation with relativity cheap elements without energy intensive synthesis techniques which could lead to a cheaper and more environmental friendly product, is an additional positive aspect.

In this approach the chemistry of Cryolithionite is tuned to achieve desired material properties. Therefore, Al will be fully substituted by trivalent cations ($Na_3M_2Li_3F_{12}$ where M = Cr, Ti, V, Mn, Fe) to widen the crystal lattice. These material can potentially be used as electrode materials. In a second step parts of M will be substituted by divalent cations to add additional Li into the structure. Theoretically this should increase the Li-ion conductivity ($Na_3M_{2-x}N_xLi_{3+x}F_{12}$ where M = Al, In, Ga and N = Cu, Ca, Mg, Zn) for electrolyte material. The focus of this thesis is the solid state synthesis applied to prepare the garnet structure. Existing synthesis pathways were investigated and further developed. XRD and scanning electron microscope (SEM) with energy dispersive X-ray spectroscopy (EDX) were used for subsequent characterisation. The resulting materials showed higher purities than previous findings.

Kurzfassung

Mit wachsendem Anteil an Erneuerbaren Energien im Energiemix ergibt sich eine neue Problematik, die der Energiespeicherung. Eine Möglichkeit zur Speicherung von elektrischer Energie sind herkömmliche Lithium-Ionen Batterien mit Flüssig-Elektrolyten. Diese Technologie birgt aber viele Nachteile: teure Dichtungsmittel, ein hohes Sicherheitsrisiko sowie geringe Energie- und Leistungsdichte. Neueste Studien zeigen, dass viele dieser Probleme durch den Einsatz von Festkörperbatterien gelöst werden könnten. Um die momentanen technischen Limitierungen dieser neuen Technologie zu überwinden muss aktiv an neuen Materialien geforscht werden. Diese Arbeit behandelt die chemische Herstellung von Kryolithionit ($Na_3Al_2Li_3F_{12}$) das in natürlicher Form in Grönland vorkommt. Eine synthetisch modifizierte Kryolithionit Struktur birgt das Potenzial einer hohen Li-Ionen Leitfähigkeit und einer hohen elektrochemischen Stabilität und könnte somit maßgeblichen Einfluss in der Entwicklung der nächsten Generation von Festkörperbatterien haben. Weitere positive Faktoren sind die kostengünstigen Ausgangsmaterialien und der relativ geringe Energieaufwand in der Herstellung.

Um die gewünschten Materialeigenschaften zu erhalten wird die chemische Zusammensetzung von Kryolithionit mithilfe eines weiterentwickelten Festkörpersyntheseverfahrens verändert. Dafür wird in einem ersten Schritt Al durch dreiwertige Kationen ($Na_3M_2Li_3F_{12}$ wenn M = Cr, Ti, V, Mn, Fe, In, Ga) dies soll eine Aufweitung des Kristallgitters bewirken. Die resultierenden Materialien könnten sich potenziell als Elektrodenmaterial eignen. Weiters kann dieses als Basis zur Herstellung eines Elektrolyt-Materials dienen. Dazu ist es notwendig, einen Teil von M mit zweiwertigen Kationen ($Na_3M_{2-x}N_xLi_{3+x}F_{12}$ wenn M = Al, In, Ga und N = Cu, Ca, Mg, Zn) zu substituieren um die Li-Ionen Leitfähigkeit zu erhöhen. Die synthetisierten Materialien werden mithilfe von Röntgendiffraktometrie, Rasterelektronenmikroskopie und Röntgenmikroanalytik charakterisiert. Im Vergleich zu bisher dokumentierten Ergebnissen konnten durch die optimierte Festkörpersynthese Produkte mit weniger Nebenphasen erzielt werden.

Contents

Affidavit . . . 3
Acknowledgement . . . 4
Abstract . . . 5
Kurzfassung . . . 6
List of Abbreviations . . . 13

1. Introduction **15**

2. Theory **17**
2.1. Basic Principle of a Galvanic Element . . . 17
2.1.1. Function of a Battery on the Example of a Li-ion Battery . . . 17
2.2. All Solid State Batteries . . . 18
2.3. Ionic Conductivity in Solid State Electrolytes . . . 19
2.3.1. Types of Defects . . . 20
2.3.2. Defect Concentration . . . 22
2.3.3. Lattice Disorder and Association of Defects . . . 23
2.3.4. Mechanism of Ion Transport . . . 23
2.4. Electrode Material . . . 25
2.4.1. Cathode . . . 25
2.4.2. Anode . . . 26
2.5. Electrolyte Material . . . 27
2.6. Garnets . . . 28
2.6.1. Structure of Garnets . . . 29
2.6.2. Cryolithionite . . . 33
2.6.3. Synthetic Fluoride Garnets . . . 33

3. Hypothesis **35**

4. Methods **37**
4.1. Solid State Synthesis 37
4.2. X-ray Powder Diffraction 38
4.3. Scanning Electron Microscopy 40

5. Experimental **42**

6. Results and Discussion **44**
6.1. Reproduction of Existing Solid State Synthesis 44
6.1.1. Synthesis,according to Langley and Sturegeon 44
6.1.2. Synthesis, according to Massa, Post and Babel 46
6.2. Modification and Refinement of Solid State Synthesis 48
6.2.1. Electrode Material 48
6.2.2. Electrolyte Material 58
6.3. Lattice Constant 76

7. Summary and Outlook **78**

A. Appendix **84**

List of Figures

1. Assembly of a Li-ion battery [1] 18
2. Examples of point defects that can be found in a pure crystal compound MX, with impurity atoms (L = metal; S = non-metal) [2, p.6] 21
3. Potential and specific capacity of cathode and anode materials [3, p.4] 27
4. Garnet Structure 30
5. Illustration of Li-ion diffusion in Li-stuffed oxide garnets [4] 32
6. Cryolithionit [5] 33
7. Bragg's law [5] 39
8. Interaction of electrons with a solid specimen [6] 41
9. Sample Preparation for XRD-analysis 42
10. XRD-pattern, reproduction of synthesis by Langley and Sturegeon T = 900 °C 45
11. XRD-pattern, reproduction of synthesis by Langley and Sturegeon T = 850 °C 46
12. image of sample after synthesis by Langley and Sturegeon 46
13. XRD-pattern, reproduction of synthesis by Massa, Post and Babel 47
14. image of sample after synthesis by Massa, Post and Babel 48
15. XRD-pattern, $Na_3Ti_2Li_3F_{12}$ (NTiL) milled and unmilled 49
16. XRD-pattern, NTiL, temperature variation 50
17. image of NTiL pellet 50
18. XRD-pattern, $Na_3Cr_2Li_3F_{12}$ (NCrL) milled and unmilled 51
19. XRD-pattern, NCrL, temperature variation 52
20. XRD-pattern, NCrL, comparison Ni-tube/Cu-tube 52
21. image NCrL pellet 53
22. XRD-pattern, $Na_3V_2Li_3F_{12}$ (NVL) milled and unmilled 54
23. XRD-pattern, NVL, temperature variation 55
24. XRD-pattern, $Na_3Fe_2Li_3F_{12}$ (NFeL), temperature variation 56
25. XRD-pattern, $Na_3Mn_2Li_3F_{12}$ (NMnL), temperature variation 57

26. XRD-pattern, $Na_3Al_2Li_3F_{12}$ (NAlL) milled and unmilled 58
27. XRD-pattern, NAlL, temperature variation 59
28. XRD-pattern of multiple NAlL pellets in Cu-tube 60
29. XRD-pattern of NAlL samples with multiple sinter steps 61
30. XRD-pattern of NAlL doped samples 61
31. XRD-pattern, $Na_3In_2Li_3F_{12}$ (NInL) milled and unmilled 62
32. XRD-pattern, NInL, temperature variation 63
33. image of NInL pellets sintered at different temperatures 63
34. NInL comparison of one sinter step and two sinter steps, sinter time 15 h and sinter temperature 600 °C. One sample stayed in the glove box (GB) between sinter steps, the other one was opened at room atmosphere [7] 64
35. XRD-pattern of a NInL sample doped with CaF_2 65
36. SEM image of NInL doped with 0.1 CaF_2 66
37. SEM image of a NInL pellet doped with 0.1 CaF_2, EDX analysis 66
38. XRD-pattern of a NInL samples doped with CaF_2 with multiple sinter steps 68
39. XRD-pattern of a NInL sample doped with MgF_2 69
40. SEM image of NInL doped with 0.1 MgF_2 69
41. SEM image of a NInL pellet doped with 0.1 MgF_2, EDX analysis 70
42. XRD-pattern of a NInL samples doped with MgF_2 with multiple sinter steps 71
43. XRD-pattern comparing NInL samples doped with MgF_2 sintered in different crucibles (Ni-tube/Cu-tube) 72
44. XRD pattern of NInL doped with 0.1 CuF_2 73
45. XRD pattern of NInL doped with 0.1 ZnF_2 73
46. XRD-pattern, $Na_3Ga_2Li_3F_{12}$ (NGaL), temperature variation 74
47. XRD pattern of NGaL doped with 0.1 MgF_2 with additional LiF 75
48. XRD-pattern of a NGaL samples with multiple sinter steps 76

49. Synthesis Process 78

List of Tables

1. Ions Used for Lattice Parameter Equation $X_3Y_2Z_3Q_{12}$ [8] 31

2. EDX Spectra of NInL doped with 0.1 CaF_2 67
3. EDX Spectra of NInL doped with 0.1 MgF_2 70
4. Lattice Constant 77

5. Best Sinter Temperature for Fluoride Garnets 79

6. Used Chemicals 84
7. Weight of Chemicals 17.4.2018 84
8. Weight of Chemicals 23.4.2018 85
9. Weight of Chemicals 14.5.2018 with 10% more LiF 85
10. Weight of Chemicals 05.06.2018 85
11. Weight of Chemicals 23.7.2018 85
12. Weight of Chemicals 17.10.2018 85
13. Weight of Chemicals 06.11.2018 85
14. Weight of Chemicals 07.11.2018 86
15. Weight of Chemicals 08.11.2018 86
16. Weight of Chemicals 15.11.2018 86
17. Weight of Chemicals 19.11.2018 86
18. Weight of Chemicals 30.11.2018 86
19. Weight of Chemicals 14.12.2018 86
20. Weight of Chemicals 17.01.2019 86
21. Weight of Chemicals 22.01.2019 86
22. Weight of Chemicals 06.03.2019 87
23. Weight of Chemicals 12.03.2019 87
24. Weight of Chemicals 14.03.2019 87
25. Weight of Chemicals 4.42019 with 10% ; 15% and 20% more LiF 87
26. Weight of Chemicals 26.04.2019 87

27. Weight of Chemicals 15.05.2019 87
28. Weight of Chemicals 23.05.2019 87
29. Weight of Chemicals 12.06.2019 88

List of Abbreviations

ASSB	all solid state battery
LiB	lithium-ion battery
SSE	solid state electrolyte
NASICON	Na superionic conductors
LISICON	Li superionic conductors
XRD	X-ray powder diffraction
SEM	scanning electron microscope
EDX	energy dispersive X-ray spectroscopy
BSE	backscattered electrons
SE	secondary electrons
NTiL	$Na_3Ti_2Li_3F_{12}$
NCrL	$Na_3Cr_2Li_3F_{12}$
NAlL	$Na_3Al_2Li_3F_{12}$
NVL	$Na_3V_2Li_3F_{12}$
NInL	$Na_3In_2Li_3F_{12}$
NGaL	$Na_3Ga_2Li_3F_{12}$
NMnL	$Na_3Mn_2Li_3F_{12}$
NFeL	$Na_3Fe_2Li_3F_{12}$
DTA	differential thermal analysis
GB	glove box
rpm	revolutions per minute
ICSD	Inorganic Crystal Structure Database

LLZO $Li_7La_3Zr_3O_{12}$

SQUID superconducting quantum interference device

CV cyclic voltammetry

GCPL galvanostatic cycling

1. Introduction

Climate change and increasing pollution forces our society to look for alternative energy sources and to minimize or vacate fossil energy use [3, p.V]. Therefore, one solution are renewable energies such as wind, water and solar energy. In comparison to combustion and nuclear power plants, which can produce a contentious baseload, renewable energies produce energy peaks which have to be stored until needed. Various solutions address this problem. One of the most effective technologies are batteries. Especially rechargeable batteries promise to restore energy by touch of a button. In a battery, the electrical energy input is stored through a conversion into chemical energy [3, p.V][9, p.XI].

The history of batteries is far from finished. It started around 1800 when A. Volta introduced the voltaic pile. Nevertheless it took another 65 years for G. Laclanche to receive a patent for his primary element. The development and research of primary as well as secondary elements were quite slow over the years. Around 50 years ago a new idea emerged at the TU Munich: lithium batteries [9, XI]. In 1991 the first lithium-ion battery (LiB) was launched by Sony. During the last 30 years LiBs have been the most promising solution. The development of those cells increased rapidly and they are now used in most mobile devices such as cellphones, laptops and power tools. Current challenges of the industry include developing safe and cheap systems with a higher energy/power density as well as higher cycling life. To meet all these criteria is not feasible and has resulted in a high pressure on the industry and development and research institutions [3, p.V].

Today LiBs are a fully developed product for portable systems. In order to increase the performance of the conventional storage system, a dramatic change of cell chemistry has to be made. One appealing solution is the usage of inorganic solid state electrolytes (SSEs) instead of organic electrolytes [3, p.311]. In ASSBs the currently used organic electrolytes, which are highly flammable, are replaced with an SSE that has a higher thermal stability. Another advantage for SSEs are the better mechanical properties which increase the safety of the battery as well. Dead weight for packaging for liquid electrolytes can be re-

duced with ASSBs, substantially increasing energy density. Inorganic SSEs present a higher electrochemical stability window, and therefore are usable with high potential cathode materials which increase the energy density resulting in a further performance improvement [10].

Several different SSEs have been reported already (see Chapter 2.4.), one auspicious material are garnets (see Chapter 2.5.). The garnet structure is given as $X_3Y_2Z_3Q_{12}$ where X, Y, and Z are cations with the coordination number of 8, 6 and 4. Q represents the anion, which could be O^{2-} or F^- [11]. The currently most promising solid Li-ion electrolytes are garnet-type metal oxides Li-ion electrolytes. For example, $Li_{6.4}La_3Zr_{1.4}Ta_{0.6}O_{12}$ shows a bulk Li-ion conductivity of 10^{-3} Scm^{-1} at room temperature [12]. During this thesis another group of garnets was investigated, fluoride garnets.

One up to now not considered material is Cryolithionite. Fluoride garnets occur in nature only in one chemical composition, the mineral Cryolithionite ($Na_3Al_2Li_3F_{12}$) for which the trivalent metal ion is aluminium (see Chapter 2.6.2) [13]. Cryolithionite has a wide electrochemical stable widow however, the Li-ion conductivity is very low. For this thesis, it is hypothesized that Cryolithionite can be crystal chemically engineered to exceed the capabilities of current available electrolytes by a high Li-ion conductivity and a wider electrochemical stable window. Therefore, Al will be fully substituted by trivalent cations ($Na_3M_2Li_3F_{12}$ where M = Cr, Ti, V, Mn, Fe) to widen the crystal lattice. These material can potentially be used as electrode materials. In a second step parts of M will be substituted by divalent cations to add additional Li into the structure. Theoretically this should increase the Li-ion conductivity ($Na_3M_{2-x}N_xLi_{3+x}F_{12}$ where M = Al, In, Ga and N = Cu, Ca, Mg, Zn) for electrolyte material.

Different approaches to synthesize this garnets have been attempted, with a fluid synthesis, HF gase and a solid state synthesis in the 1970s. All of the reported attempts showed a high amount of impurity phases in the resulting material (see Chapter 2.6.3). The goal of this work was to reproduce and optimize the solid state synthesis in order to prepare materials with a high purity for both electrode and electrolyte material.

2. Theory

The following theory section should give a brief overview of the basic knowledge, such as, the functionality of a battery, mechanisms of solid state conductivity, materials used in solid state batteries and the garnet structure.

2.1. Basic Principle of a Galvanic Element

A galvanic element contains two electrodes, an electrolyte and in case of fluid electrolytes a separator between the electrodes. Usually the active mass is saved in an electrode structure or is the electrode itself [14, p.482-483].

If the current that was saved in the active mass is exhausted, there are two possibilities [14, p.482-483]:

- If the applied voltage is reversed, the electrode reaction takes place in the other direction which reloads the element. This is called a secondary element [14, p.483].
- For a primary element one or both electrodes can not be reloaded [14, p.483].

2.1.1. Function of a Battery on the Example of a Li-ion Battery

The function of a battery is explained by the principle of a Li-ion battery. The left electrode consists of a layered structure, for example, $Li_xMO_2(M = Co^{4+(-x)}, Ni^{4+(-x)}, Mn^{4+(-x)})$ $O-M-O-Li-O-$ layers alternate. This structure can store reversible Li-ions. Materials for the other electrode could be, for example, nanocrystaline amorphous silicon, $Li_4Ti_5O_12$, $LiAl$, Li_22Sn_5 and LiC_6 [15].

A ceramic membrane is placed between the two electrodes to separate the half cells. The electrolyte usually comprises an aprotic solution or polymer containing $LiClO_4$ or $LiPF_6$ as

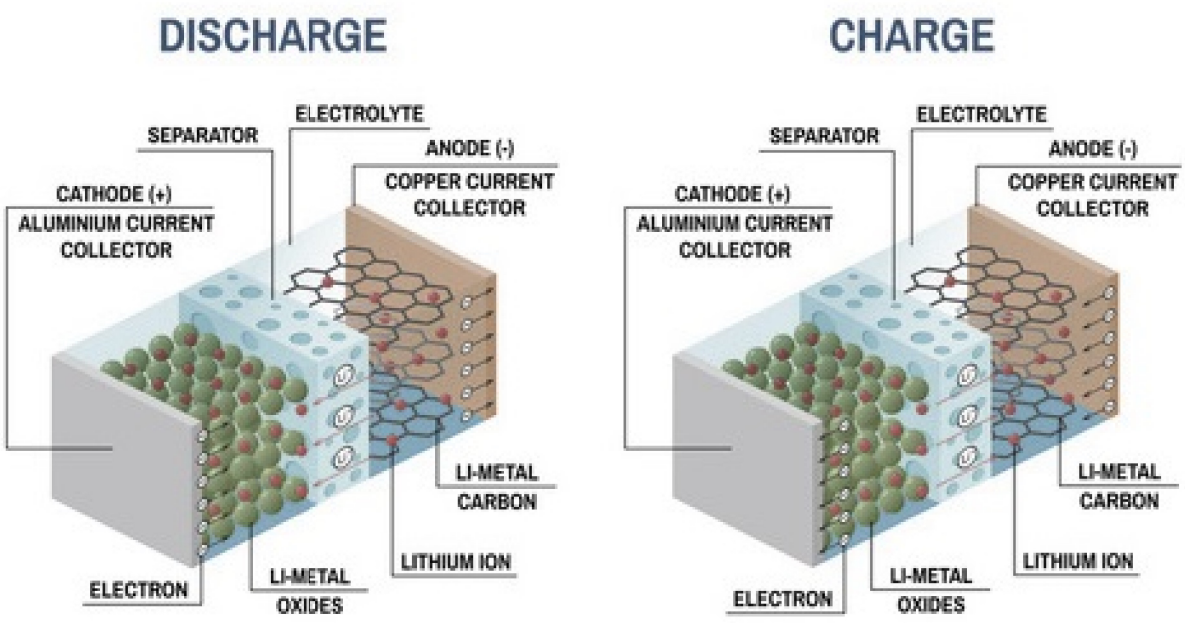

Figure 1.: Assembly of a Li-ion battery [1]

a transfer agent for Li^+ [15].

During discharging the following reaction occurs on the anode side [15]:

$$Li_xC_{6x} \leftrightarrow C_{6x} + xLi^+ + xe^- \tag{2.1}$$

and on the cathode side [15]:

$$Li_{1-x}MO_2 + xe^- + xLi^+ \leftrightarrow LiMO_2 \tag{2.2}$$

therefore, a reversible exchange of Li-ions is performed between the two electrodes [15].

2.2. All Solid State Batteries

The principal functionality of an ASSB is similar to a conventional Li-Ion liquid-battery. However, the liquid electrolyte is substituted by a solid material. One cell includes an anode, a cathode and a solid state electrolyte. The anode is attached to a copper foil to reduce the internal resistance. When the battery is charging, Li-ions of the $LiCoO_2$ crystal move towards the electrolyte interface and then cross through the electrolyte over to the carbon

layer in the anode. During discharging the reverse process takes place [16].

Solid state batteries have some advantages compared to liquid cells. The design can be simplified therefore dead weight can be avoided. This results in a higher energy density. Inorganic SSEs are electrochemically more stable than polymer electrolytes or organic liquid electrolytes. Solid state electrolytes can be paired with higher potential cathode material which further improves energy density. These cells are safer than commercial batteries, owing to their non-flammability and better mechanical properties [10].

Although there are a lot of advantages associated with this technology, also a few drawbacks still exist. At the moment SSEs are not usable in low and ambient temperature conditions and the power and current output is less than from liquid cells. This is caused by the large resistance of the SSE at room temperature to ionic conductivity. Another issue is the stress created at ambient or room temperature at the electrode-electrolyte interface due to discontinuous contact [16].

2.3. Ionic Conductivity in Solid State Electrolytes

The ionic conductivity in a solid electrolyte is induced by defects or disorders. Any ionic compound with a perfect crystal structure would be an isolator. Due to the type of defect, the super ionic solids can be classified [2, p.4]:

- point defects (zero dimensional), concentration of defects $10^{20} cm^{-3}$
- molten sub lattice types: liquid-like sub-lattice, the number of ions of a particular type is smaller than the number of sites. The number of ionic charge carrier is $10^{20} cm^{-3}$ for these materials.

In a solid lattice anions and cations can move. The movement of cations is preferential on account of their smaller ionic radius. A wide range of super ionic solids are cation conducting, for example, Li^+, Na^+, K^+. Another aspect that many solid electrolytes have in common, is the involvement of a monovalent ion, caused by the strong Coulomb interaction between divalent or trivalent ions within the lattice [2, p.5, 6].

2.3.1. Types of Defects

To describe lattice defects in an ionic solid the Kroger-Vink notation is used. This notation provides information of the nature, location and effective charge of a defect, relative to the natural unperturbed lattice. Taking into consideration the variety of point defects (see Figure 2) in an ionic crystal (MX; M and X are monovalent) as well as their charge neutrality, they can be summed up as follows [2, p.5]:

- Vacancies: in a pure binary compound an M^+ ion is missing from its original site described as $V_X^{'}$. On the other hand, a missing vacant anion site is described as $V_X^{\cdot}$ (V =vacancy, prime = effective native charge, dot= effective positive charge) [2, p.5].
- Interstitials: An ion M^+ or X^- appears in an interstitial site $M_i^{\cdot}$ or $X_i^{'}$. This kind of defect (vacancy, interstitial) occurs when in one area of the material a particle is missing or when there is an additional one. Both cases cause a distortion of the lattice in the immediate neighborhood [2, p.5].
- Antisite defects: M occurs in an X site or the other way around. M_X or X_M [2, p.6].
- Schottky defect: In this case a cation and an anion are missing in the lattice ($V_M^{'}$, $V_X^{\cdot}$), the positive and negative ions leave their normal sites to jump into vacancies [2, p.5, 6].
- Frenkel defect: When a cation interstitial and vacancy occurs ($V_M^{'}$, $M_i^{\cdot}$) in a material at the same time, it is called the Frenkel defect. The Anti-Frenkel defect ($V_X^{\cdot}, X_i^{'}$) describes the same scenario with anions. Two different migrations of atoms can take place. When interstitials jump from interstice to interstice, this is called an interstitial mechanism. Secondly, interstitials can also jump to a normal site pushing the atom to another interstitial. This is called interstitialic mechanism [2, p.6].
- Impurities: A substitution of a normal or interstitial site with a different valet atom [2, p.6].

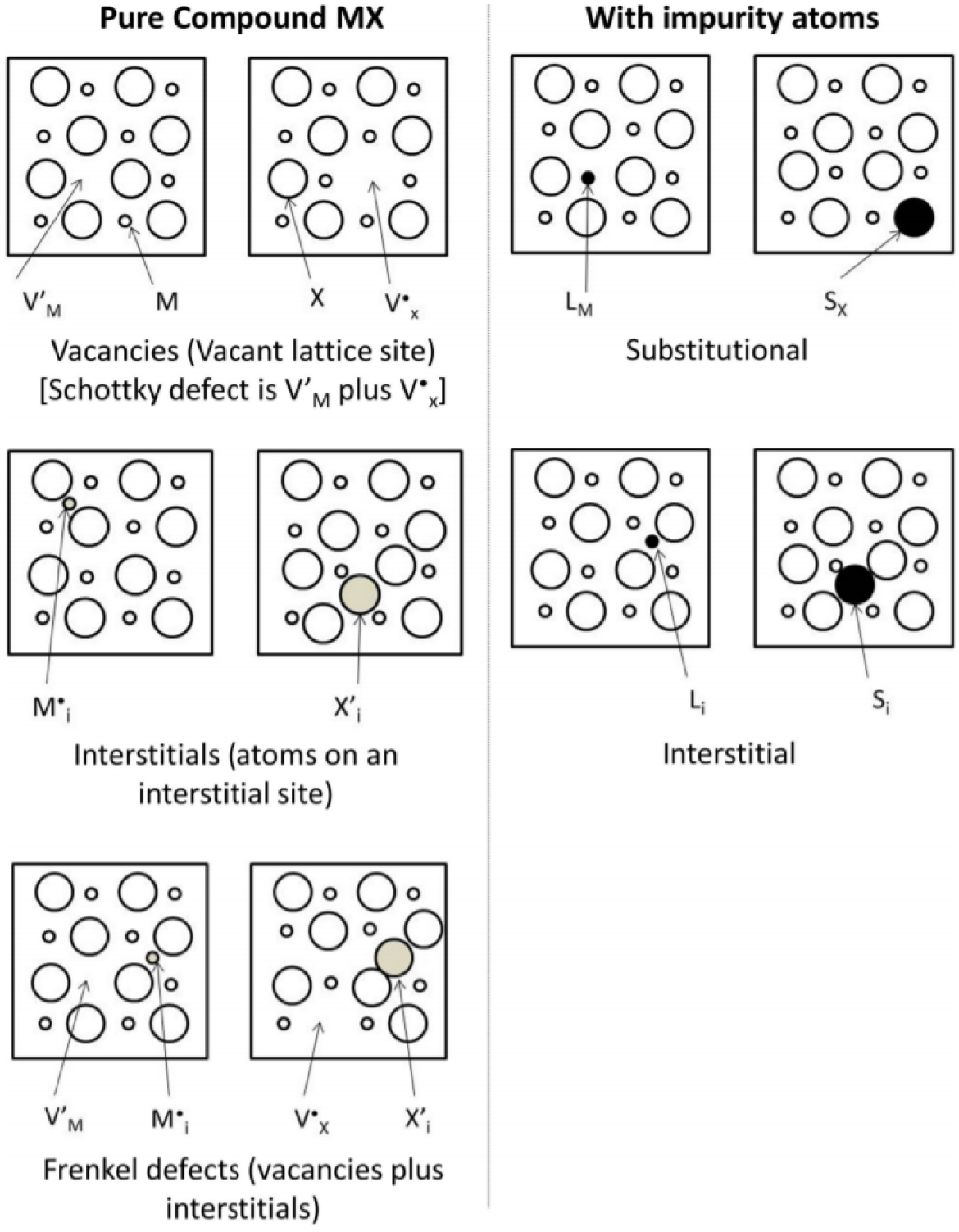

Figure 2.: Examples of point defects that can be found in a pure crystal compound MX, with impurity atoms (L = metal; S = non-metal) [2, p.6]

.

2.3.2. Defect Concentration

The concentration of defects is necessary, in order to specify ionic conductivity or the diffusion. By using thermodynamic parameters Schottky- and Frenkel-type concentration of defects can be described [2, p.7].

Pure Crystal

The Schottky defects can be described with the positive and negative ion vacancies by x_1 and x_2 and their number n_+ and n_- [2, p.7]:

$$n_+ = n_- = N \exp(\frac{-G_S}{kT}) \tag{2.3}$$

$$x_1 x_2 = x_0^2 = \exp(\frac{-G_S}{kT}) \tag{2.4}$$

$$= \exp(\frac{S_S}{K}) \exp(\frac{-H_S}{kT}) \tag{2.5}$$

where G_S, S_S, and H_S are the Gibbs energy, entropy and enthalpy of the formation of a Schottky pair. N represents the number of anions and cations [2, p.7].

The same kind of expression can be found for the Frenkel defect [2, p.7]:

$$n_F = (NN')^{1/2} \exp(\frac{-G_F}{2kT}) \tag{2.6}$$

In this case N' is the number of interstitial sites and G_F is the Gibbs energy to form a Frenkel defect [2, p.7].

Doped Crystal

If a normal atom in the lattice is substituted by a aliovalent impurity, this crystal is doped. Additional cation vacancies occur in order to compensate the charge difference [2, p.7].

$$x_1 = x_2 + c_1 \tag{2.7}$$

in this case c_1 describes the mole fraction of the divalent impurity. When adopting Equations 2.5 and 2.7, the following expressions can be found [2, p.7]:

$$x_1 = \frac{1}{2c_1}((1 + (\frac{2x_0}{c_1}^2)^{1/2} + 1) \tag{2.8}$$

$$x_2 = \frac{1}{2c_1}((1 + (\frac{2x_0}{c_1}^2)^{1/2} - 1) \tag{2.9}$$

In case of a divalent anion, with an impurity concentration of c_2, the charge neutrality always has to be preserved [2, p.8]:

$$x_1 + c_2 = x_2 \tag{2.10}$$

therefore x_1 and x_2 can be characterised with the following equations [2, p.9]:

$$x_1 = \frac{1}{2c_2}((1 + (\frac{2x_0}{c_2}^2)^{1/2} - 1) \tag{2.11}$$

$$x_2 = \frac{1}{2c_2}((1 + (\frac{2x_0}{c_2}^2)^{1/2} + 1) \tag{2.12}$$

2.3.3. Lattice Disorder and Association of Defects

Apart from point defects lattice disorder can also be associated with defect. These disorders can be isotropic, in one direction, in two directions or in a layered structure. When aliovalent impurities are included in a lattice, they are usually distributed randomly. Electrostatic attraction resulting of these defects may form defect pairs or large clusters that could be electrically neutral or carry a net charge. These effects cause a not linear increase in conduction. For instance, in doped material there is a maximum concentration of doping. After that point a new secondary face is built [2, p.9, 10].

2.3.4. Mechanism of Ion Transport

In a solid electrolyte the random movement in all possible directions of ions is permanent. The movement from a lattice point, for instance, to a vacancy or interstitial site, happens without an electric field. The density of defects in the crystal is uniformly distributed. By applying an electric field the ions migrate in one direction but still move randomly. This diffusion and migration of ions through defects is the basic process of ionic conductivity in a crystalline ionic solid [2, p.14].

The Jumping Mechanism

During ionic conduction and diffusion, the ions jump through the lattice. This is called a jumping process. The transport of ions happens through defects, a direct cation-anion exchange can not happen. The probability of an ion to jump into a defect describes the ion transport. This can be proportional to [2, p.15]:

- the probability for an ion to jump into a defect in a given unit time and direction is described by the jump frequency [2, p.15]
- the probability of having a defect in the neighborhood, is described by the product of the number of the nearest neighbor sites and the mole fraction of the defects [2, p.15].

The jumping frequency ω depends on the potential barrier experienced by the ion. When the Einstein Model is applicable, the harmonic vibration of the ion around their equilibrium position variates with frequency, ν_0. This can be expressed with the following equation [2, p.15]:

$$\omega = \nu_0 \exp(\frac{-\Delta G}{kT}) \tag{2.13}$$

In this case the system is at a thermodynamic equilibrium with an equal probability of jumps in either direction. If an electric field (E) is applied, the potential energy experienced by the interstitial ion jumping from one interstitial to another is asymmetric. This can be described with the following equation [2, p.15]:

$$\omega = \nu_0 \exp(-(\Delta G - \frac{\frac{1}{2}qaE}{kT}) \tag{2.14}$$

where q is the charge of the interstitial ion and a is the inter ionic distance [2, p.15].

Diffusion

In any solid material with a concentration gradient, diffusion results in a net ionic flux into the direction in which it tends to make the concentration uniform. Fick's first law (one dimensional) [17, p.126]:

$$J_x = -D(\frac{dC}{dx}) \tag{2.15}$$

where D (how many particles go throw an area x in a certain time) is the diffusion coefficient. This term is negative due to a positive diffusion flux resulting from a negative concentration gradient [17, p.126].

If the diffusion is three dimensional in x, y, z direction, the equation has to be expanded with ∇c (vector concentration gradient) [17, p.127]:

$$j = -D\nabla c \tag{2.16}$$

If the diffusion is anisotropic, D has to be represented as a tensor with the combination of the First Fick's Law and the continuity equation results in the Second Fick's Law [17, p.127]:

$$\frac{dc}{dt} = \nabla(D\nabla c) \tag{2.17}$$

2.4. Electrode Material

2.4.1. Cathode

In an ASSB, the cathode material is important because it provides the battery with the needed ions during charging. This material requires a very stable structure to overcome the charging and discharging process [16]. A good ionic conductivity of the cathode material is essential, due the transference of ions across the cathode during the charge and discharge process [10].

Today metal oxides are most commonly used in [16][10]:

- piled arrangements, such as $LiMO_2$ (M = Co, Ni, Mn, or their mixtures) [10]
- spinal arrangements LiM_2O_4 (M = Mn or a mixture with Co or Ni) [10]
- olivine $LiMPO_4$ (M = Fe, Mn, Ni, Co and their mixture) [10]

A layered arrangement, for instance $LiCoO_2$, is used in many cases. It is suitable for the lithiation/delithiation process and has a good specific energy (150 $mAhg^{-1}$). This material is quite expensive to produce, especially when cobalt is involved. The spinal arrangement has a small resistance for the passage of lithium ions during the charging and discharging process. Nevertheless it experiences a notable phase change during ion transfer resulting in less stability and lower capacity than $LiCoO_2$. The olivine based structure allows the

transfer of ions at a low resistance, on the other hand it has a high self discharge rate of phosphorus. Generally, the performance of ASSBs is still limited by the cathode materials at the moment (see Figure 3) because of the low specific capacity. To overcome these limitations experiments with nano crystalline materials have been conducted. They exhibit better properties but also create more safety issues [16].

In the last decades a devoted effort has been made to develop high specific capacity and high voltage cathodes. Lithium enriched layered solid solutions ($Li_2MnO_3 - LiMO_2$) are of special interest for the development of next generation of batteries. For this material the electrochemically inactive Li_2MnO_3 phase stabilizes the layered $LiMO_2$ providing a wide range of operating voltages. These solid solutions show a specific capacity of 250 $mAhg^{-1}$ between 2 and 4.8 V verses Li/Li^+. The major drawbacks of these layered structures are high irreversible capacity (40-100 $mAhg^{-1}$) in the first cycle, an increase of voltage hysteresis (delay) with cycling, and a poor rate capability. Spinal and olivine structured material have been intensively studied as well. These materials show high operating voltages and three dimensional fast Li^+ ion diffusion. Nevertheless these high operating voltages trigger the formation of impurity phases. A majority of the problems are associated with the oxidative decomposition of the electrolyte solvent on the surface of the high voltage cathode particles, leading to dissolution(active material loss), low coulombic efficiency and uncontrollable growth of resistive surface layers [3, p.6-8].

2.4.2. Anode

Anode materials require a high Li/Li^+ storage capacity. During the charging process the Li-ions need to be stored in the material. Most commonly used substances for anodes are carbon or carbon based materials as well as graphite. These materials bring a variety of advantages as they can absorb a lot of Li-ions and withstand large numbers of charging and discharging cycles. To improve the capacity of graphite the material can be doped. The low capacity of the carbon is currently the most central issue [16].

$Li_4Ti_5O_{12}$ has a spinal structure and can also be used as an anode material. This material has a very stable cycling stability, excellent safety properties and very good reversibility. Nevertheless the material has also a few drawbacks, for example, the destructive gases that are generated during the charging and discharging process as well as the relatively low elec-

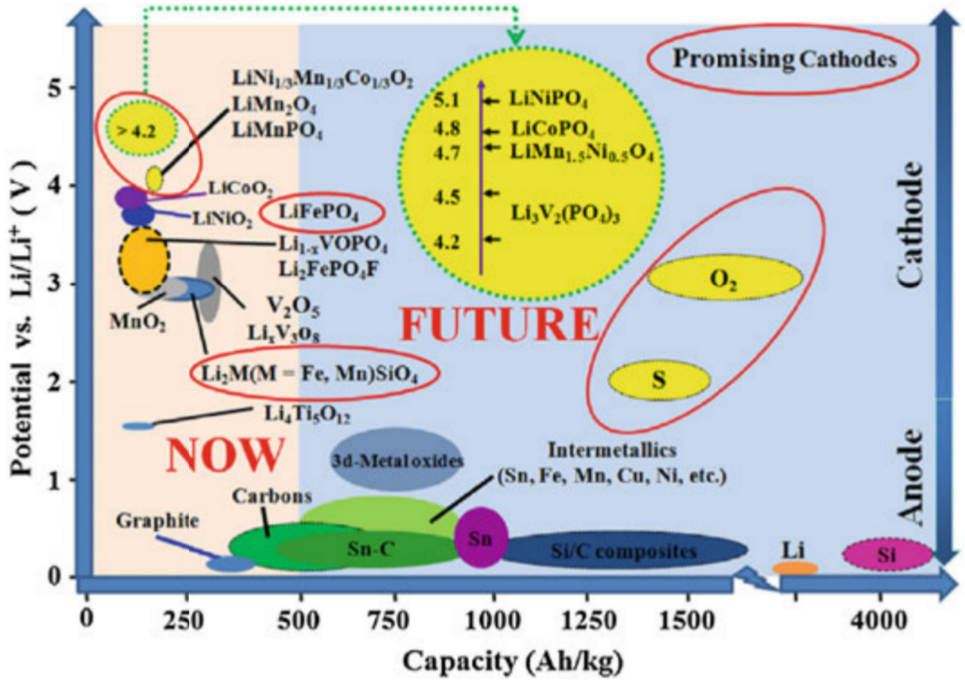

Figure 3.: Potential and specific capacity of cathode and anode materials [3, p.4]

tronic conductivity [3, p.10].

Li-alloys (Sn, Si, Ge) are also sometimes applied because of their very good capacity (see Figure 3) and suitable operating potential. The biggest issue with Li-alloys is the poor cycling stability due to the dramatic volume change during charging and discharging which leads to material pulverization and inter particular contact loss [3, p.10].

Pure Li can be used as well, it has a good cycling stability and capacity (see Figure 3) but can only be used at room temperature [16].

2.5. Electrolyte Material

SSEs should fulfill several essential requirements [10]:

- high total (bulk and grain-boundary) ion conductivity of $10^{-2} Scm^{-1}$ [12].
- a broad chemical and electrochemical stable window to use high voltage cathodes up to 6 V as well as Li and Li-alloys as anode material [12].

- the electrolyte should be chemically stable against anode and cathode during operating and during manufacturing, to prohibit side reaction at the electrode-electrolyte interface [12].
- low electrode-electrolyte interface charge-transfer resistance [12].

There are three categories of solid state electrolytes: ceramics, glasses and solvent free polymer electrolytes. The most promising class are ceramics [3, p.312].

Na superionic conductors (NASICON) Li-ion conductors have the general formation of $LiA_2(PO_4)_3$ $(A = Ti, Zr, Ge, Hf)$. These types of materials crystallize in a rhomboidal three-dimensional network structure (space group $R-3c$) characterised by a large tunnel perpendicular to the c axis. There are two sites available for Li-ions to diffuse. The best performance shows $Li_{1.3}Al_{0.3}Ti_{1.7}(PO_4)_3$ with 3 x 10^{-3} $\Omega^{-1}cm^{-1}$. This material is unstable towards Li metal anodes due to the facile respectability of Ti^{4+} [3, p.318].

The main representative of Li superionic conductors (LISICON) is $Li_{14}ZnGe_4O_{16}$. The structure is a 3D skeleton where lithium ions are in four different sites, two sites are interstitial sites where the Li-ions are highly mobile. The conductivity of these materials at room temperature is very low but improves rapidly with increasing temperature [3, p.318]. On the other hand, they have a good chemical and electrochemical stability [10].

Perovskite-type electrolytes were first prepared with the following chemical structure $Li_{3x}La_{2/3-x}TiO_3$. This structure shows a total conductivity of 2 x $10^{-5}Scm^{-1}$ at room temperature, which is not good enough yet. The material is not electrochemically stable below 1.8 V vs. Li/Li^+, which makes it incompatible with many low potential anodes. Other compositions with $Li_{3/8}Sr_{7/16}Ta_{3/4}Zr_{1/4}O_3$ were found. The conductivity for them improved by one magnitude. Their degree of stability to low voltages is higher (1.0 V vs. L/Li^+) [10].

2.6. Garnets

Garnets are a well-known mineral supergroup. They have a very attractive crystal structure and are quite common. Natural garnets appear in magmatic and metamorphic rocks. The pressure and temperature conditions during the forming process of the garnets are reflected in the crystal chemistry and structure. Garnets are not only appealing for mineral collectors

or jewellers because of their appearance but are also interesting for modern research because of their physical and chemical properties. Besides already existing applications, such as YAG lasers, the material is gaining interest for the usage as solid electrolyte material [4].

2.6.1. Structure of Garnets

The German mineralogist and crystallographer Georg Menzer was the first person to solve the crystal structure of garnets in 1925 [4]. This was the first silicate mineral that was solved. Garnets are part of the cubic system and show the $Ia\bar{3}d$ space group (this is the space group with the highest symmetry). The general structure of a garnet is $X_3Y_2Z_3Q_{12}$, but the chemical composition of the garnet varies, compare Table 1. X represents an eightfold-coordinated cation located at position $24c$. At this point the coordination polyhedron is described as triangular dodecahedron with a site symmetry 222, this can be seen as distorted cube. For Y a sixfold-coordinated cation is found located at the $16a$ position where the coordinating anions form an octahedron with a site symmetry of $\bar{3}$. The last cation (Z) is a fourfold coordination cation, located at $24d$ position. With a side symmetry of $\bar{4}$. At position $96h$ the anions (Q) are located [4]. In Figure 4 garnet structure is shown.
In nature garnets have been investigated as these minerals play an important role in geo-scientific. The International Mineralogical Association introduced the term of the "garnet supergroup" to classify the different kinds of natural garnets systematically. This term does not only include the common garnet group, silicate garnets, but also minerals from other chemical classes, such as vanadates, oxides, arsenates and fluorides, which are isostructural with classic silicate garnets. The garnet supergroup includes 32 approved species of natural occurring garnet-type structures and 5 additional species needing further studies [4].

Synthetic garnets are already used in many applications, see above. One particular group, oxide garnets, show very compelling results regarding Li-ion conductivity. These materials were first identified by Thangadurai et al. in 2003 [4]. After that a number of additional garnet-type Li-conductors with different compositions have been discovered. A majority of these structures are based on the cubic garnet structure with space group $Ia\bar{3}d$, a few chemical compositions of this group actually show structures with lower symmetries. In comparison to other garnets, garnet-type Li-ion conductors contain more than three Li-ions per formula unit at the tetrahedral site. Consequently, these Li-stuffed oxide garnets exhibit exceptional ionic conductivity (up to 10^{-3} Scm^{-1}) at room temperature. Additionally, they also show outstanding chemical and electrochemical stability, as they are stable against

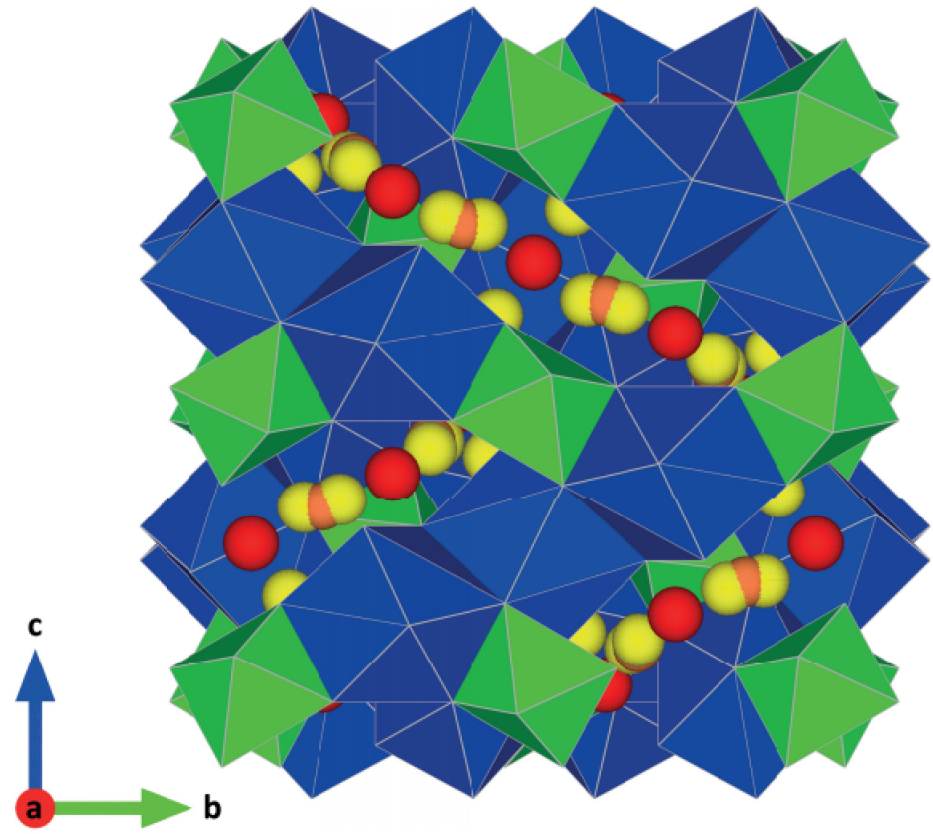

Figure 4.: Garnet Structure: Illustration of a Li-stuffed oxide garnet. Blue LaO_8 dodecahedra with La^{3+} located position 24c; and green ZrO_6 octahedra with Zr^{4+} located at the 16a site. Li^+ is located on 3 different positions which are partially occupied: In red the conventional occupied 24d position, in orange 48g and in yellow 96h, represented by yellow spheres [4].

Table 1.: Ions Used for Lattice Parameter Equation $X_3Y_2Z_3Q_{12}$ [8]

X	M^{+}:	Li,Na, K, Ag, Tl
	M^{2+} :	Mg, Ca, Sr, Mn, Fe, Co, Cd, Pb
	M^{3+} :	Sc, Y, La, Pr, Nd, Sm, Eu, Cd, Tb, dy, Ho, Er, Tm Yb, Lu, In Bi
	M^{4+} :	Zr, Hf
Y	M^{+} :	Li, Na
	M^{2+} :	Mg, Ca, Mn, Fe, Co, Ni, Cu, Zn, Cd
	M^{3+} :	Sc, Y, Dy, Ho, Er, Tm, Yb, Lu, Ti, V, Cr, Mn, Fe, Co, Ni, Rh, Al, Ga, In
	M^{4+} :	Ti, Zr, Hf, Ru, Sn
	M^{5+} :	Nb, Ta, Sb
	M^{6+} :	Te
Z	M^{+}:	Li
	M^{2+} :	Co, Zn, Cd
	M^{3+} :	Fe, Al, Ga
	M^{4+} :	Ti, Si, Ge, Sn
	M^{5+} :	V, Nb, As
Q	O^{2-} :	F^{-}

metallic Li and display a wide electrochemical stable window up to 6 V [4].

As already mentioned above, Li-stuffed oxide garnets incorporate more than three cations at the tetrahedral site to accomplish charge balance. The adjustment of the Li-content can be made by changing the valence of the X and Y cations. The additional Li-ions are located at two interstitial sites, these sites are not occupied in the common garnet structure. The first interstitial site is the sixfold-coordinated $48g$ site of the space group $Ia\bar{3}d$, with point symmetry 2.

The second site is an additional distorted fourfold-coordinated $96h$ site, with a space group equal to the other interstitial site $Ia\bar{3}d$ and a point symmetry 1. This side can be described as the split position of the $48g$ site, due to a slight displacement of Li^{+} at the $48g$ site. The coordination polyhedron of the $96h$ site is normally described as strongly distorted LiO_4 tetrahedron. Owning to the electrostatic interaction between Li^{+} cations, the occupation of the sixfold-coordinated Li^{+} site is not possible if both neighbouring tetrahedral $24d$ sites

are taken up. This leads to a limitation of 7.5 Li^+ per formula unit. From a structural standpoint, every LiO_4 polyhedron, which host a Li^+ on the $48g$ site, connects to two LiO_4 tetrahedra with Li^+ at the $24d$ site by phase sharing. Additionally, each LiO_4 tetrahedra is connected with four LiO_6 polyhedra by shared faces, see Figure 5. The result is a three-dimensional polyhedron network made up by alternating $LiO_4(24d) - LiO_6(48g)$ polyhedra, which are only partially occupied by Li^+. This results in a fast Li-ion conduction. The diffusion path is shown in Figure 5, $24d - 96h - 48g - 96h - 24d$ [4].

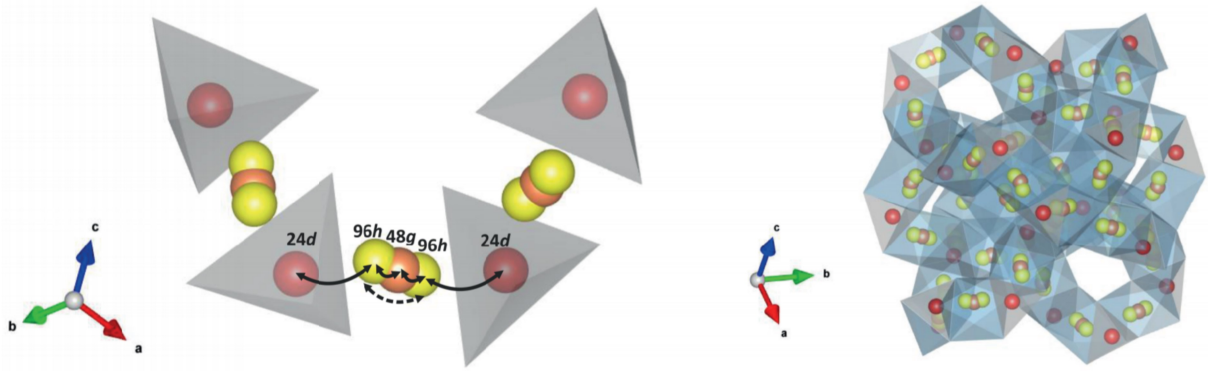

Figure 5.: Illustration of Li-ion diffusion in Li-stuffed oxide garnets [4]

The most promising Li-ion stuffed oxide garnet is $Li_7La_3Zr_3O_{12}$ (LLZO), showing a ionic conductivity of about 3 x 10^{-3} Scm^{-1} at room temperature. For this material the grain boundary resistance was found to be less than 50 %, resulting in a bulk ionic conductivity at the same magnitude as the total ionic conductivity. Later Geiger et al. discover that this garnet structure exhibits a phase transition from tetragonal to cubic at 100 - 150 °C. The ionic conductivity of the cubic phase is higher than of the tetragonal phase. Thus, a stabilisation of the cubic phase at room temperature is essential. By doping of this chemical composition with a variety of elements, the properties could be improved up to a conductivity of 1.62 x10^{-3} Scm^{-1} for $Li_{6.20}Ga_{0.30}La_{2.95}Rb_{0.05}Zr_2O_{12}$ at room temperature. Nevertheless, these types of garnets are not stable at ambient atmosphere due to moisture and CO_2 and are not able to withstand high voltages. Therefore, they can not be used in combination with high voltage cathode material [3].

2.6.2. Cryolithionite

Cryolithionite ($Na_3Al_2Li_3F_{12}$) is the only naturally occurring fluoride garnet. This mineral can be found in Greenland. Small pieces (centimetre or decimetre scale) of this structure are usually embedded in Cryolite (Na_3AlF_6). The first investigated specimen of Cryolithionite was obtained in Ivigtut, Greenland. A closer investigation of this findings showed a lattice parameter of $a = 12.122 \pm 0.002$ Å and a longer tetrahedral cation - anion (Li^+-F^-) distance of 1.846 ± 0.003 Å than the octahedral cation-anion (Al^{3+}-F^-) distance of 1.807 ± 0.003Å. This is unique for a garnet group. In an utter arranged structure, the cations Na^+, Al^{3+} and Li^+ are located in the positions 24c, 16a and 24d, in each case of the space group $Ia\bar{3}d$. In the general position 96h the fluoride ions can be found [18].

Figure 6.: Cryolithionit [5]

2.6.3. Synthetic Fluoride Garnets

After investigating the natural occurring Cryolitionite, a variety of syntheses have been introduced to reproduce and modify the mineral in a lab. The first attempts to reproduce a fluoride garnet ($Na_3M_2Li_3F_{12}$ where M = Cr, Ti, Al ect.) was made in 1967 by R. Pape et al For the synthesize a solid state reaction under HF gas was used [19]. In 1976 an aqueous solution was used for the reaction to synthesize fluoride garnets. During this experiment a variety of chemical compositions with the formula $Na_3M_2Li_3F_{12}$ (where M = Cr, Ti, Al, Mn, Co, Ni) was prepared. However, the syntheses where M = Mn, Co, Ni were not successful, for M = Fe and Cr water molecules were incorporated in the structure [20]. This synthetic modified materials were investigated with a battery of material characterisations, such as Mössbauer spectroscopy, infrared spectroscopy, differential thermal analysis (DTA), superconducting quantum interference device (SQUID)-analysis and EDX. A few years later two different solid state synthesis procedures were published. The first one used transition-metals where M (M = Sc, Ti, V, Cr, Fe , Co, Rh, Ga and In). This approach was successful

for each chemical composition except for Rh. However, the resulting materials exhibited a high amount of impurities [13]. The other solid state approach investigated one chemical composition, $Na_3Fe_2Li_3F_{12}$. For this method an extra drying step under high vacuum was added. The resulting material was characterised and its properties were compared with Cryolithionit. The distances between the positions in the crystal structure were similar, nevertheless, the spacings for $Na_3Fe_2Li_3F_{12}$ were found to be wider. For example $Fe - F$ = 192.9 pm compared to $Al - F$ = 180.7 pm, due to the larger ion radius [21].

3. Hypothesis

In this approach the chemistry of Cryolithionite is modified to achieve the desirable properties for the application is a solid state battery. Modified Cryolithionite has the potential to overcome current limitations of SSE by combining high Li-ion conductivity and a high electrochemical stability. Nevertheless unmodified Cryolithionite has a very low conductivity. This method will focus on the substitution of Al with other elements to increase the amount of additional Li^+ in the structure. This method is expected to lead to rapid Li^+ transport between the electrodes enabling facile inserting and removing Li^+ during charge and discharge.

In a first step, similar to previous publications (see Chapter 2.6.3), the trivalent metal ion is fully replaced by transitions metals, this should widen the crystal lattice of the garnet structure. These materials could be subsequently used as electrode material. Goldschmidt's rule shows that the full exchange of a cation with a radius difference less than 15 % and a charge difference less than 1 is possible. Therefore it should be possible to substitute the elements and still gain the garnet structure.

$$Al^{3+} \leftrightarrow M^{3+} \tag{3.1}$$

Chemical compositions where M = Ti, V, Cr, Mn, and Fe are attempted.

For the electrolyte material the M position is altered by using In and Ga. In 1964 and 1966 Mill was able to successfully synthesis $Ca_3In_2Si_2O_{12}$ and $Ca_3In_2Si_2O_{12}$. His findings should be also applicable for $Na_3M_2Li_3F_{12}$ where M = In and Ga [22].

Naturally occurring Cryolithionite has a very low conductivity similar to oxide garnets. By increasing the amount of Li^+ in oxide garnet per unit formula the conductivity rose exponentially until the crystal structure was not able to accommodate any additional Li^+ (see Chapter 2.6.1). In order to increase the amount of Li^+ in the formula a fraction of M is replaced by sub-valet cations.

$$Na_3[M_{2x-y}N_y]Li_{3+y}F_{12}$$
$$M = Ga, Al, In$$
$$N = Cu, Ca, Mg, Zn$$

4. Methods

The objective of this work is to synthesise high conducting and electrochemical stable solid electrolyte and electrolyte material by syntactically engineering the Cryolithionit structure. For this purpose a solid state synthesis (see Chapter 4.1) was used. Additionally, XRD (see Chapter 4.2), SEM and EDX (see Chapter 4.3) were utilized for the material characterisation. These techniques were essential for the adjustments and optimization of the method.

4.1. Solid State Synthesis

A variety of methods can be applied to synthesise inorganic solids. Some can be prepared by a range of routes, others are much more difficult and require special methods [23, p.187].

The simplest, and oldest method is called shake 'n bake or, beat 'n heat. For this method the powdered reactants are mixed together, pressed into pellets or some other shape and then heated in a furnace for a certain period of time. This method is not very sophisticated, however, very efficient. The reaction speed is intrinsically slow for this method. The reactants may be well mixed at the level of individual particles (e.g. on a scale of 1 μm) nevertheless, on an atomic scale they are very inhomogeneous. To achieve a homogeneous mixture at that scale, either solid state counter diffusion of ions between different particles or liquid/gas-phase transport is necessary [23, p.188].

In a solid state synthesis the grains of the educts have to be homogeneously mixed and in contact with each other to form the desired product. First of all, nucleation of small crystals with the spinel stoichiometry and structure has to take place. Therefore, stable nuclei have to form. In order for a nuclei to be stable and not disintegrated spontaneously as soon as it is formed it has to be significantly larger then a single unit cell. Thus, it contain many many tens of atoms. The critical size of nuclei is a balance between the positive surface energy and the negative free energy of the formation. For very small nuclei the surface-area-to-volume

ratio is too large resulting in unstable nuclei. Nucleations are challenging due to the large number of ions that must get together with the correct arrangement to form a stable nucleus [23, p.188, 191].

A solid state reaction requires chemically reactive starting materials and/or easily diffusing ions in the mixture. Possibly occurring difficulties are the loss of reactants by evaporation or reactivity with the container. When planing a solid state synthesis there are four main issues to consider: choice of starting materials, mixing method, container and heat treatment conditions [23, p.188, 191].

The starting material should be ideally of accurately known stoichiometry, as pure as possible and reactive. Some materials show sensitivity to water and/or CO_2 in the atmosphere or contain transition elements in uncertain or mixed valence states. Therefore, reactants may have to be dried or be kept in a GB. To facilitate a solid state reaction, it is essential to bring the particles of the reactants into contact and increase the surface area. In respect thereof, samples are mixed and milled, manually or mechanically. When using for example ball milling there is a danger of contamination by the milling media. Another issue is to choose the right container depending on the atmospheric sensitivity of the product and educt as well as the reactivity of the sample. In a last step the right firing schedule has to be elected. Therefore, a few points should be considered:

- a smooth decomposition of any oxy salts reagents without excessive frothing, melting or leakage of reagents from the container
- no melting and in particular volatilisation of one or more of the reactants
- temperatures at which the reactants react together at a reasonable time scale
- suitable atmosphere for the reaction [23, p. 192]

4.2. X-ray Powder Diffraction

With the help of this technique a fast analysis of the crystal phases of the samples could be made.

In 1912, Max von Laue first reported that crystalline substances act as three dimensional diffraction grids for X-ray wavelengths similar to the spacing of planes in crystal lattices.

The basic principle of XRD is constructive interference of a monochromatic X-ray and a crystalline sample. A cathode ray tube produces X-rays which then are filtered through a monochromator and collimated to concentrate before directed towards the sample. When the sample interacts with the X-rays, the interaction is either constructive or destructive. Consequently, constructive interaction is obtained when fulfilling Bragg's law [24].

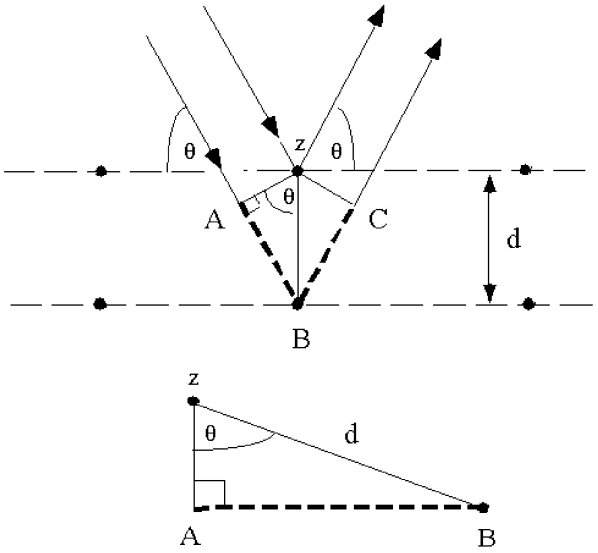

Figure 7.: Bragg's law [5]

Bragg's law (see Equation 4.1) relates the wavelength of the electromagnetic radiation ($lanbda$) to the lattice spacing (d) and diffraction angle (θ) in the crystalline sample. The beam scans over the sample through a range of 2θ angles, the constructively diffracted X-rays are counted by a collector. All possible diffraction directions of the lattice should be obtained because of the powder sample. The diffraction peaks are then converted to d-spacing to identify the material. Each material has a unique set of d-spacing [24].

$$n\lambda = 2d \sin\theta \tag{4.1}$$

XRD is assembled out of an X-ray tube, a sample holder and an X-ray detector. A filament is heated up in a cathode ray tube to produce electrons. The electrons are accelerated towards a target material by applying a voltage. The electrons require enough energy to dislodge inner shell electrons of the target material. When this gap is filled by an electron of a higher shell, the energy difference is released as a characteristic X-ray. The most common components in the spectra are K_α and K_β. These wavelengths are characteristics of the target materials

(Cu, Fe, Mo, Cr). These X-rays are monochromated by foil or a monochrometer is directed on the sample. K_α can be divided into $K_{\alpha 1}$ and $K_{\alpha 2}$. These two wavelengths are so close to each other that an average of the two is used. When Bragg's law is fulfilled, a peak in the intensity occurs. The sample is rotated at an angle of θ in the path of the collimated X-ray beam, while the detector rotates at an angle of 2θ [24].

4.3. Scanning Electron Microscopy

In SEM a focused high-energy electron beam is used to generate a variety of signals of a solid specimen. With this method the external morphology, chemical composition and crystalline structure and orientation of the material can be determined. Through SEM a battery of different signals can be produced by electron-sample interactions [25]:

- secondary electrons (SE) are used for imaging, the image shows the topographic contrast of the sample. The information collected include the first $50nm$ of the sample. Peaks and higher areas of the sample are brighter, more SE can reach the detector, and holes or porosities appear darker [26].
- backscattered electrons (BSE) can also be used for imaging. The information extracted cover the first $100nm$ into the material. The appearing image contrast reflects the average atomic number of the area. Areas with light elements scatter less electrons to the detector and heavier elements scatter more electrons. [26].
- EDX: for this method the emitted characteristic X-rays are analysed. The characteristic X-rays of the material can be correlated with a reference spectra. The information is contracted from $1 - 3\mu m$ depth. This information can be mapped or just certain points or lines can be analysed [26].

With SEM images of 1 cm to 5 microns width can be scanned. Magnifications of 20x to 30,000x with a resolution of 50 to 100 nm can be imaged. A SEM consists of a filament to produce the electrons which are directed and focused on the samples through a series of magnetic lenses and apertures. Depending on the signal different detectors are used. [25].

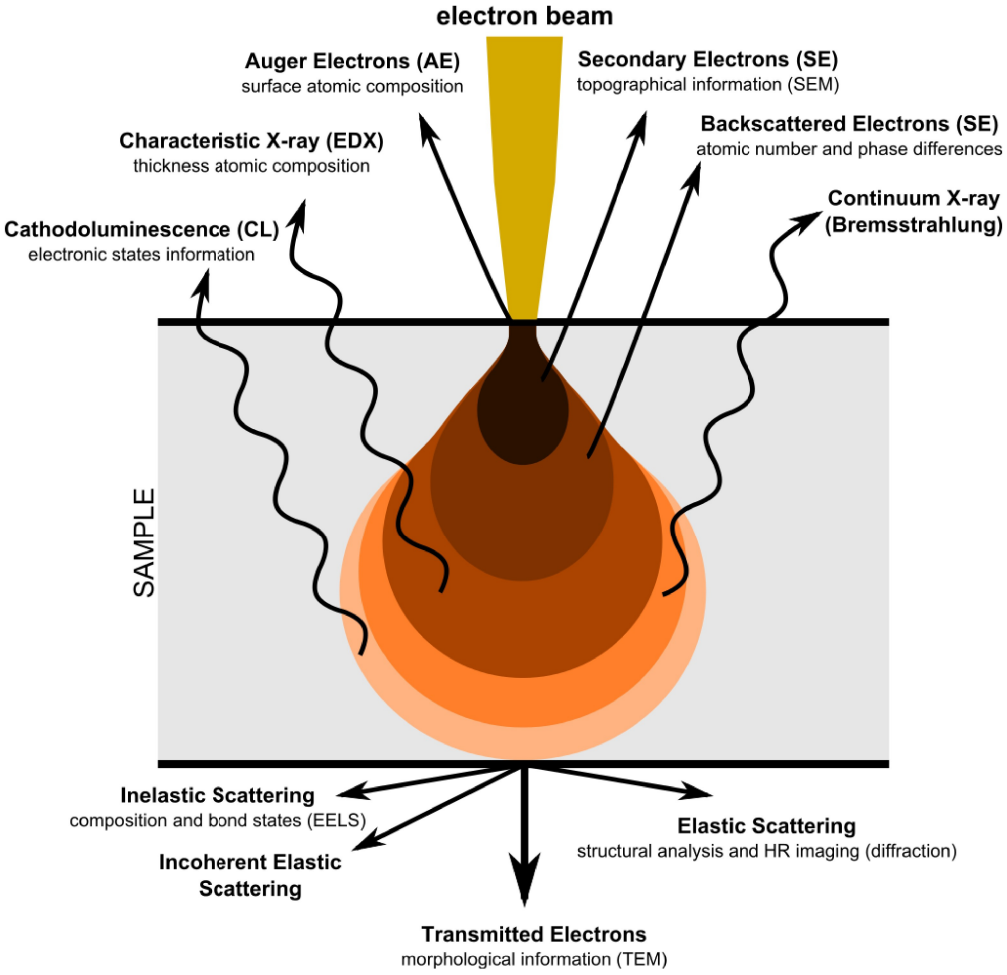

Figure 8.: Interaction of electrons with a solid specimen [6]

5. Experimental

The garnet type fluorides $Na_3M_2Li_3F_{12}$ samples were prepared by conventional solid state reaction method from stoichiometric amounts of NaF, LiF and MF_3 (M = Cr, Ti, Al, In, Mn, V, Ga and Fe). The exact weight can be found in the Appendix.

$$3NaF + 3LiF + 2MF_3 \rightarrow Na_3M_2Li_3F_{12} \tag{5.1}$$

The reactants were adjusted for the intended electrolyte materials, see Equation 5.2:

$$3NaF + (3+x)LiF + (2-x)MF_3 + xNF_2 \rightarrow Na_3M_{2-x}N_xLi_{3-x}F_{12} \tag{5.2}$$

where $M = Cr, Ti, Al, In, Mn, V, Ga, Fe$ and $N = Zn, Ca, Mg, Cu$.

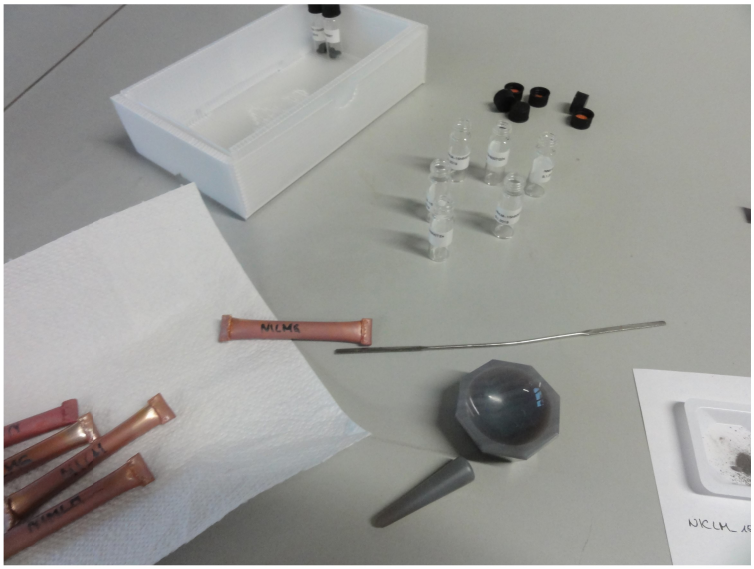

Figure 9.: Sample Preparation for XRD-analysis

Preparation of the samples differed for each experiment. The reactants were mixed (with a mortar or ball milling). For the mechanical milling process a planet micro mill by Fritsch was used. The chemical components were milled for 6 min. then rested for 6 min. This

procedure was repeated 12 times with a velocity of 500 revolutions per minute (rpm). After milling the material was pressed into pellets (5 nm or 8 nm) before placing them in a crucible (Cu- or Ni-tube). The reactants are highly reactive with air therefore these crucibles were chosen and the samples were prepared under argon atmosphere in a GB. The pellets were then heated in a furnace under argon atmosphere with a heating rate of 5 °C/min. After the reaction time the materials were allowed to slowly cool down to ambient temperature.

The characterisation of the prepared samples were performed by XRD using CuKα radiation with 2θ range from 10 to 90°. The chemical compositions and morphology of the cross-section of sintered samples were analysed using SEM and XRD.

6. Results and Discussion

6.1. Reproduction of Existing Solid State Synthesis

In the following sections the reproduction of two previous reported methods are discussed.

6.1.1. Synthesis,according to Langley and Sturegeon

Richard H. Langley and George D. Sturgeon [13] used a very simple approach for their solid state synthesis of fluoride garnets. The educts are manually mixed with a morter and placed into the Cu-tube. Then the samples are sintered at 800 °C. The instructions in the paper are not very clear therefore first attempts were not successful. In the beginning, the Cu-tubes (5 mm) were too short. They experienced tearing during the reaction, thus, the samples could decompose. As an adjustment longer tubes (10 mm) were introduced.

Figure 10 shows the XRD pattern of the first positive results. Two samples were sintered for 96 h at 900 °C and the third for 72 h at 900 °C. The XRD-pattern for NTiL and NAlL shows all diffraction peaks attributed with the garnet ($Ia\bar{3}d$) structure. However additional reflections of impurities are observed. NCrL shows no diffraction peaks for the cubic garnet structure, nevertheless two other phases can be identified, $NaCrF_6$ and Na_3CrF_6. Na_3AlF_6 occurs naturally around $Na_3Al_2Li_3F_{12}$ reservoirs and is called Cryolite [27]. Additionally, diffractions of the reactants NaF and LiF can be detected. Consequently, the sinter conditions were not optimal.

The XRD pattern of NVL, NTiL, NFeL and NGaL sintered at 850 °C for 48 h is shown in Figure 11. NTiL matches the theoretically found pattern in the Inorganic Crystal Structure Database (ICSD). However, a few impurities can be observed. The diffraction pattern of NVL and NFeL shows the reflections of the reference pattern, nevertheless, a high amount of impurity phases is found. The fourth sample NGaL shows no matches with the reported data of the cubic phase garnet structure (space group $Ia\bar{3}d$). Nevertheless, two other phases,

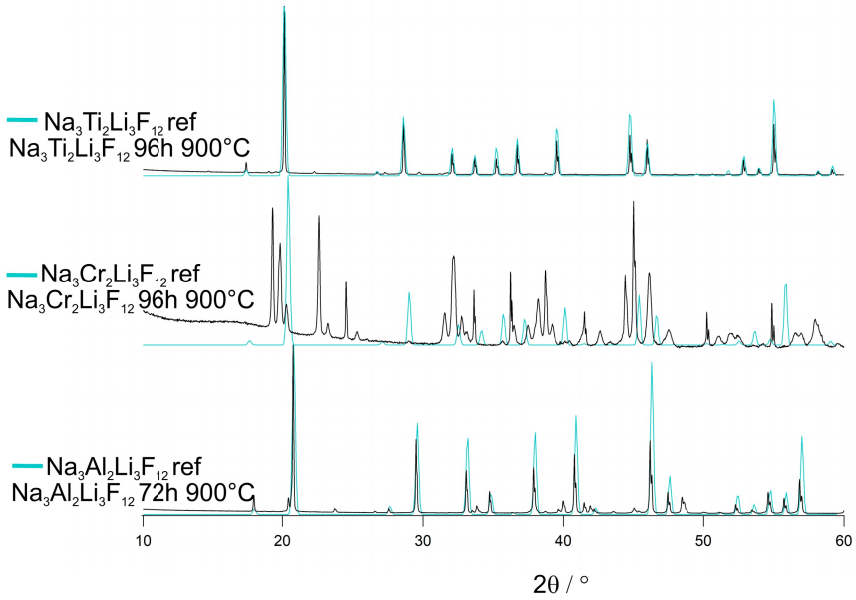

Figure 10.: XRD-pattern reproduction of synthesis by Langley and Sturegeon T = 900 °C dwelling time 72/96 h, chemical compositions: NAlL, NTiL, NCrL [7]

a monoclinic(space group $P2_1/n$) Na_3GaF_6 and LiF are identified. It is assumed that the sinter conditions were not optimal and depending on the chemical composition the optimal temperature has to be adjusted.

Figure 12 shows the image of a NTiL sample sintered for 48 h at 850 °C and a NCrL sample sintered for 96 h at 900 °C. NCrL was very difficult to extract from the tube because it was attached to the Cu-tube after the synthesis. NTiL lost the pellet form during the solid state synthesis. The temperatures seem to be too high for both chemical compositions.

Richard H. Langley and George D. Sturgeon were able to successfully synthesize with this method fluoride garnets where M = Sc, Ti, V, Cr, Mn, Fe, Co, and Ni. However, the resulting materials contained a high amount of impurity phases [13]. During this work a successful reproduction of the experiment for M = Ti, Al, V, Fe was conducted. Analogous to their findings a high amount of impurity phases was detected. For M = Cr and Mn no successful result could be obtained. It is assumed that the sinter temperatures are too high to obtain satisfying material samples.

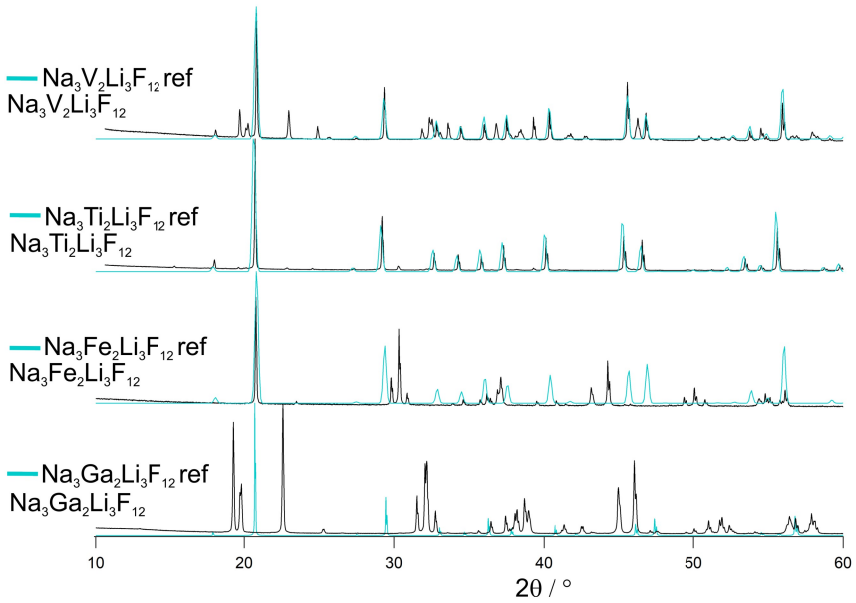

Figure 11.: XRD-pattern reproduction of synthesis by Langley and Sturegeon T = 850 °C dwelling time 48 h, chemical compositions: NVL, NTiL, NFeL, NGaL [7]

Figure 12.: image of sample after synthesis by Langley and Sturegeon, Left: NTiL sintered for 48 h at 850 °C Right: NCrL sintered for 96 h at 900 °C

6.1.2. Synthesis, according to Massa, Post and Babel

In the literature a second approach for the solid state synthesis is described. In 1982, Werner Massa, Bernhard Post and Dietrich Babel tried to synthesize a fluoride garnet where M = Fe (NFeL). They used Pt-vile and applied an additional drying step in a high vacuum chamber for 6 hours at 120 °C before sintering. The first sinter stage was at 800 °C for 60 h and the second at 850 °C for 8h [21].

For this thesis, the synthesis parameters were slightly adjusted. The samples were sintered in a Cu-tube instead of a Pt-vile. The first sinter step lasted 67 hours and the second 6 hours. Five different chemical compositions were investigated with this method.

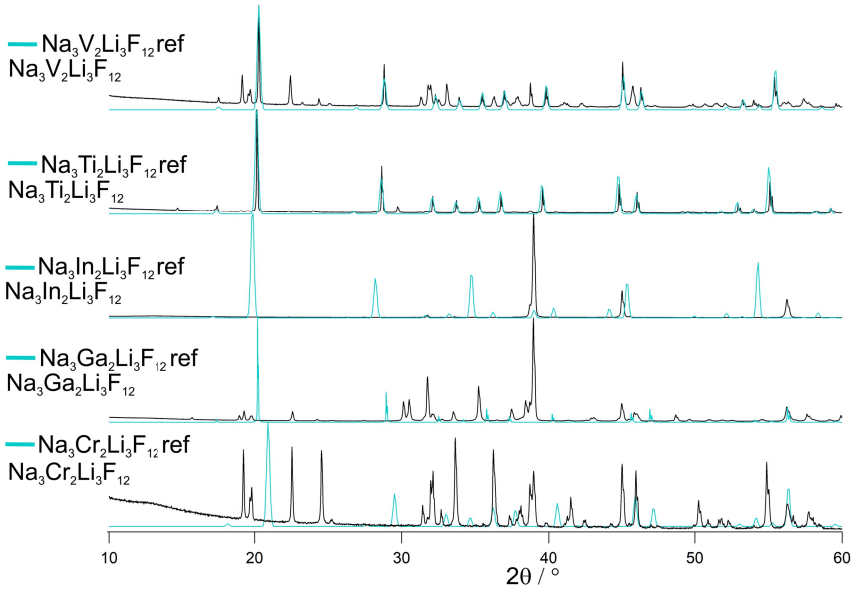

Figure 13.: XRD-pattern reproduction of synthesis by Massa, Post and Babel T = 800/850 °C dwelling time 67/6 h, chemical compositions: NVL, NTiL, NInL, NGaL, NCrL [7]

Figure 13 shows the measured XRD pattern of NVL, NTiL, NInL, NGaL and NCrL. The only chemical compositions that show a successful synthesis are NVL and NTiL. Nonetheless, NTiL exhibits a minor amount of additional reflections in comparison to NVL. The measurement of NInL shows no indication of the cubic garnet structure. The only detected phase is LiF therefore supposable remaining chemicals of the sample decomposed during the sinter process. The last two measurements seen in Figure 13 are NGaL and NCrL. In both samples the reported reflections for the fluoride garnet structure can not be found, however two other phases can be identified, LiF and Cryolite (Na_3MF_6) where the trivalent cation is Ga or Cr.

Figure 14 shows the image of NVL and NCrL dried in high vacuum at 120 °C and sintered for 67 h at 800 °C and 8 h at 850 °C. Both samples were attached to the Cu-tube and lost there pellet form after the synthesis. As previously stated, the sinter temperatures seem to be too high, possibly above their melting point.

The additional drying step for this approach shows no improvement of the samples when comparing it to the other method found in literature.

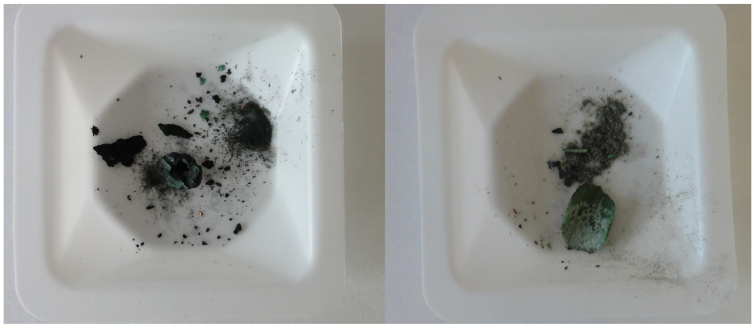

Figure 14.: image of sample after synthesis by Massa, Post and Babel, Left: NCrL sintered for 67 h at 800 °C and 8 h at 850 °C Right: NVL sintered for 67 h at 800 °C and 8 h at 850 °C

6.2. Modification and Refinement of Solid State Synthesis

Primary results indicate that the sinter conditions for each material composition are different. Thus, the impact of particle size, chemical composition, sinter temperature as well as the amount of sinter steps was analysed for each chemical variation.

6.2.1. Electrode Material

In the following sections the XRD-patterns of the potential electrode materials are shown and discussed.

NTiL

Figure 15 shows two samples sintered at 700 °C for 15 h with a chemical composition of NTiL. The impact of an additional milling step before pressing the pellets is visible, the milled samples show smaller reflections for the impurity phases. These impurity phases can be identified as Na_3TiF_6 and LiF. The second sample in Figure 15 was not milled before pressing therefore the particles of the reactants were bigger causing a smaller reaction surface. The XRD pattern shows a higher amount of impurity phases as well as an additional phase of TiF_2. The mechanical milling step improves the purity of the sample significantly.

The measured XRD patterns in Figure 16 illustrate a comparison of NTiL sintered at different temperatures. Both samples were mechanically milled before pressing into pellets and

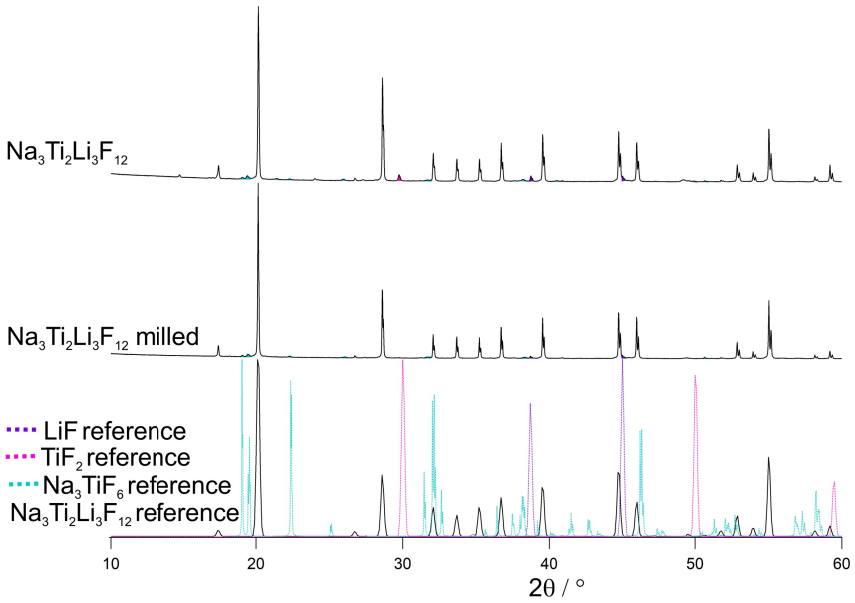

Figure 15.: XRD-pattern, NTiL milled and unmilled, T = 700 °C, dwelling time = 15 h [7]

sintered for 15 h. Primary results for NTiL (compare 6.1.1) at higher temperatures showed already good results therefore this narrow temperature range for the experiment was chosen. The XRD pattern of the sample sintered at 600 °C shows the reflections for the cubic garnet structure. Nonetheless, four additional impurity phases are found. Similar to the unmilled sample in Figure 15 LiF, TiF_2 and Na_3TiF_6 are detected as well as a supplementary phase, CuF_2. Thus, this sample shows a detectable interaction with the crucible. The second pattern illustrated in Figure 16 shows the reflections of the sample sintered at 700 °C. Just a very small amount of reflections deviates from the reference pattern found for NTiL. Nevertheless, the two impurity phases detected are Na_3TiF_6 and LiF, therefore the dwelling time is possible insufficient for a full reaction.

Figure 17 shows an image of a NTiL pellet after the solid state synthesis at 700 °C for 15 h. The sample is deformed and covered in a dark layer. Under the dark layer the sample appears lavender. Langley and Sturgeon found in their experiment the same color for the resulting material. The color changes during the synthesis from brown (TiF_3) to lavender (NTiL). The resulting color of the material for the sample sintered at 600 °C is grey. However, the deformation and the dark layer would suggest a too high sinter temperature although the best results were found with these conditions.

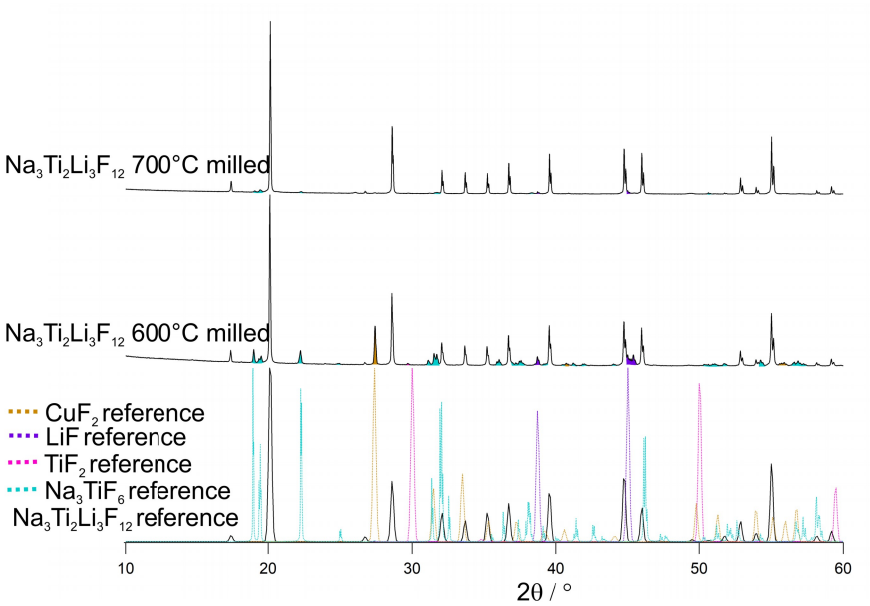

Figure 16.: NTiL, milled, dwelling time: 15 h, T = 600 °C and 700 °C [7]

Figure 17.: image of NTiL pellet after solid state synthesis, T = 700 °C, dwelling time = 15 h

NCrL

Figure 18 shows two samples sintered at 600 °C for 15 h with a chemical composition of NCrL. The impact of an additional milling step before pressing the pellets is shown. For the milled sample smaller reflections for impurity phases are detected. The first sample in Figure 18 was not milled before pressing therefore the particles of the reactants were bigger causing a lower reactive surface. Thus, the XRD pattern shows a higher amount of impurity phases. The impurities detected can be identified as Cryolite with the trivalent cation Cr and LiF. The XRD pattern of the milled sample shows a very small amount of impurity phases. However, the reflections are equal to the unmilled sample. Langley and Sturgeon found in their experiment $CrF_3H_6O_3$, this successes that during their method the samples

were not fully protected from the room atmosphere. This phase was not detected in the samples during this thesis [13].

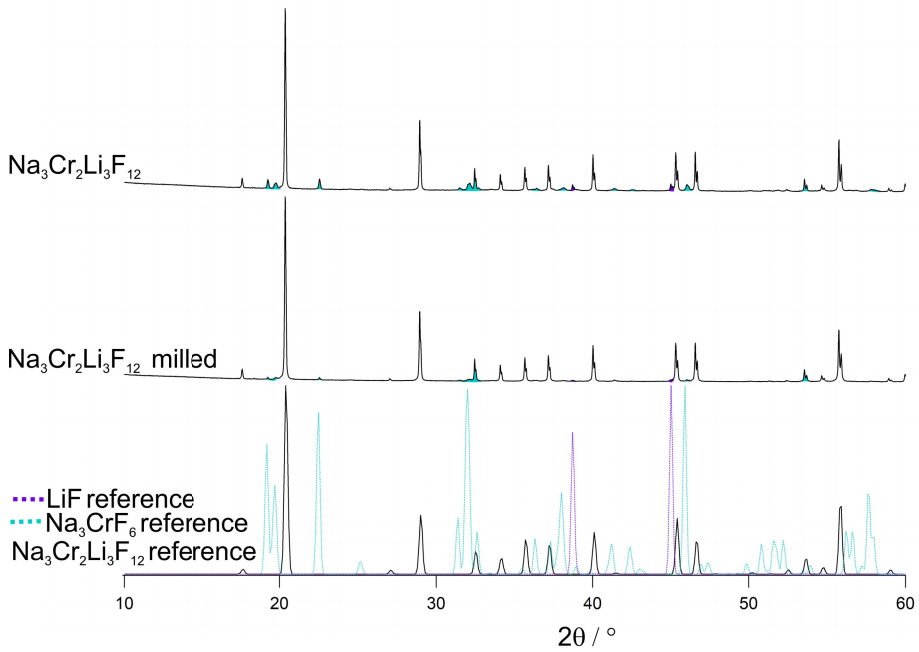

Figure 18.: XRD-pattern, NCrL milled and unmilled, T = 600 °C, dwelling time = 15 h [7]

The measured XRD patterns in Figure 19 show a comparison of NCrL sintered with two different temperatures. Both samples were mechanically milled before pressing into pellets and sintered for 15 h. During the reproduction of already existing methods (see Chapter 6.1.1) a successful synthesis was not achieved. For NCrL a DTA analysis is reported in the literature [20], where the melting point was observed at 690 °C, the sinter temperature should be below the melting point of the material. Consequently, this temperature range was used for this experiment. In the XRD pattern for the sample sintered at 700 °C the reflections for the cubic garnet structure can be detected. Nonetheless, two additional impurity phases are found, LiF and Na_3CrF_6. By decreasing the sinter temperature by 100 °C the detected reflections of the impurity phases shrink as well. Nevertheless, the impurity phases are detectable, therefore the dwelling time was supposable not sufficient for a homogeneous diffusion.

Figure 20 shows the comparison of two NCrL samples ball milled, sintered at 600 °C for 15 h with different crucibles. To investigate the interaction between the Cu-tube and the sample during the synthesis an additional material was introduced, Ni-tubes. Equal to the

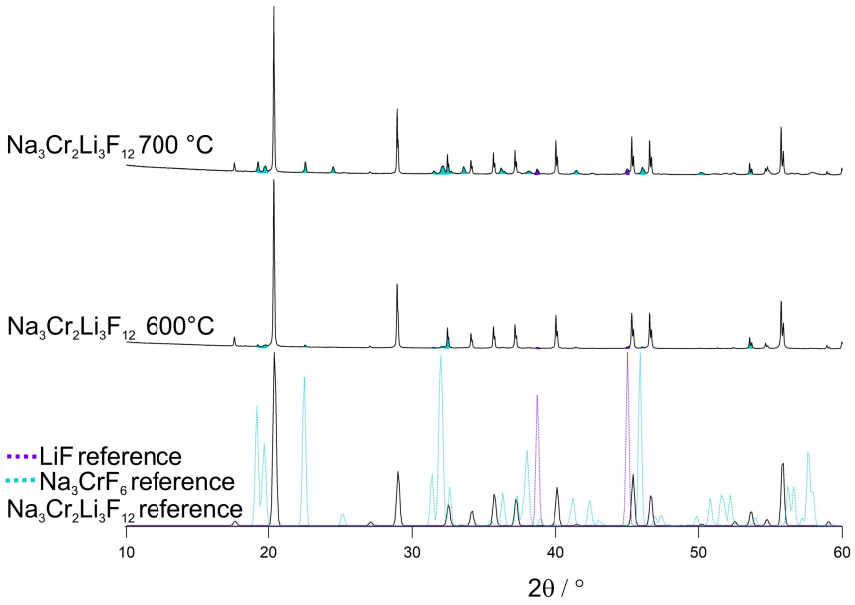

Figure 19.: NCrL, milled, dwelling time: 15 h, T = 600 °C and 700 °C [7]

measurements above two impurity phases are detected, nonetheless the amount of LiF and Na_3CrF_6 observed in either sample is equal. No additional phases are found indicating no traceable interaction.

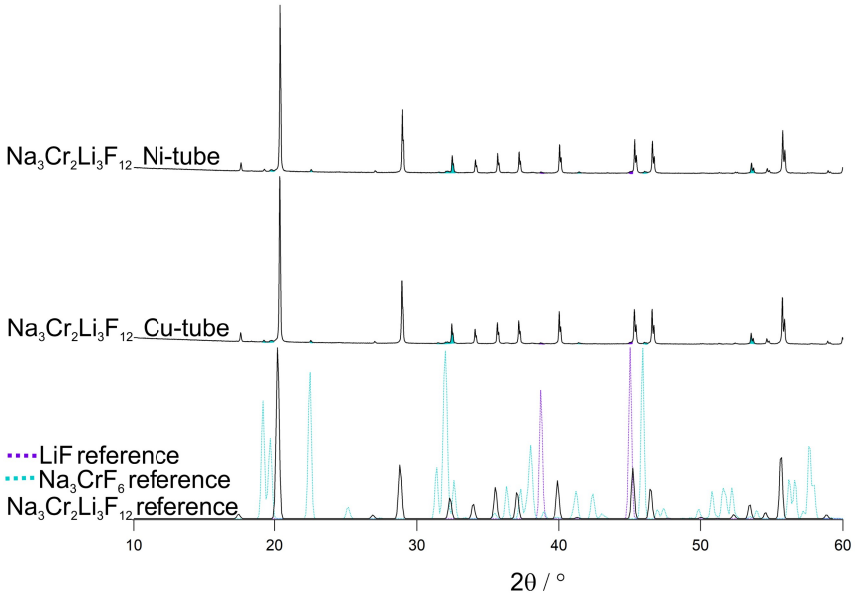

Figure 20.: XRD-pattern, NCrL, comparison Ni-tube/Cu-tube, dwelling time = 15 h, T = 600 °C [7]

Figure 21 shows an image of a NCrL pellet after the solid state synthesis at 600 °C for 15 h. During the synthesis the sample shrunk. The color changes from light green (CrF_3) to olive green (NCrL). The reported color of Cryolithionite with the trivalent cation Cr, synthesised by Langley and Sturgeon is dark green [13].

Figure 21.: image NCrL pellet after the solid state synthesis, T = 600 °C, dwelling time = 15 h

The purest sample obtained during this thesis was sintered at a temperature 200 °C lower than reported in the literature. Furthermore their is no quantitative statement about the purity state of obtained samples in the past [13]. In general the published sinter temperature appears too high emphasized by the melting point of 690 °C found in literature [20].

NVL

The XRD pattern shown in Figure 22 compares two samples sintered at 600 °C for 15 h with a chemical composition of NVL. The impact of an additional milling step before pressing the pellets is demonstrated. The XRD pattern of the milled sample shows a small amount of impurity phases. These phases can be identified as Na_3VF_6, LiF and CuF_2. The second sample in Figure 22 was not milled before pressing therefore the particles of the reactants were bigger causing a lower reactive surface. Consequently, the amount of impurities is higher. When comparing these results to previous discussed chemical compositions (NTiL and NCrL) the impurity phases are more intense and the interaction of the sample with the Cu-tube is detected for both samples. Therefore, the sinter conditions are not optimal.

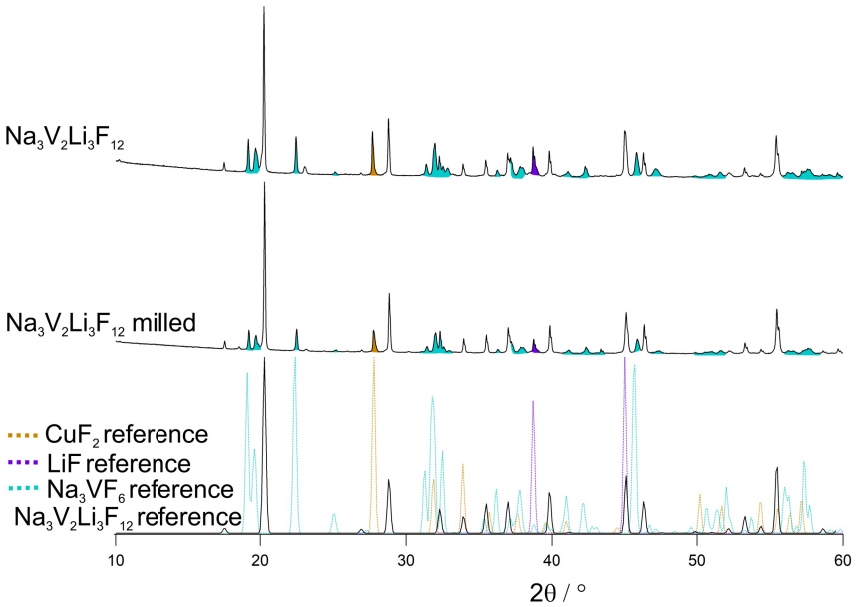

Figure 22.: XRD-pattern, NVL milled and unmilled, T = 600 °C, dwelling time = 15 h [7]

Figure 23 displays a comparison of the XRD patterns with the chemical composition of NVL sintered within a temperature range of 500 °C to 750 °C. All samples were mechanically milled before pressing into pellets and sintered for 15 h. During the reproduction of already existing methods (see Chapter 6.1.1) a successful synthesis with a high amount of impurities was attempted. This chemical composition was published once by Langley and Sturgeon [13]. They found in their experiment one impurity phase, a unidentified orthorhombic phase (a = 10.4 Å, b = 10.8 Å, c = 11.2 Å) with a sinter temperature of 800 °C. When comparing the patterns of the different temperatures in Figure 23, all sample except the one sintered

at 750 °C, contain Cryolithionite with the trivalent cation V. For each sample the same impurity phases are found, CuF_2, LiF and Na_3VF_6. However, the XRD patterns with the smallest amount of impurities is detected for the sinter temperatures of 700 °C and 500 °C.

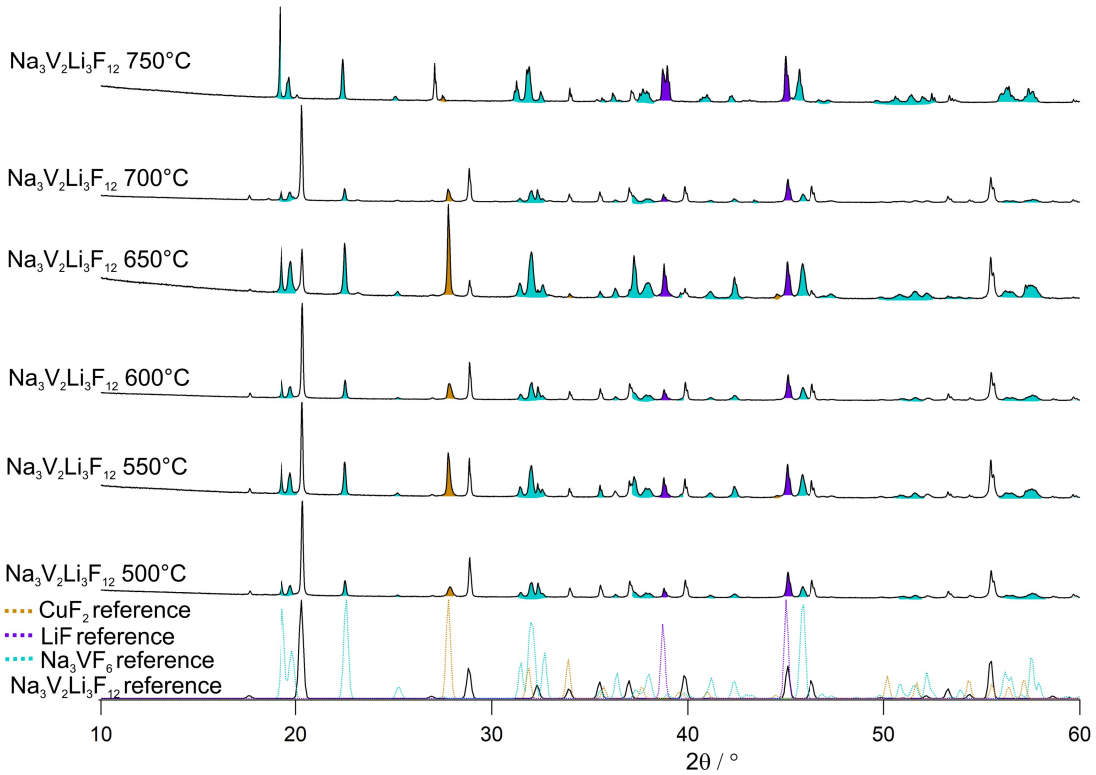

Figure 23.: NVL, milled, dwelling time: 15 h, T = 500 °C - 750 °C [7]

The color of both samples after the synthesis is equal, dark green. Langley and Sturgeon reported the color of this chemical composition as light green [13]. Nonetheless, 500 °C is probably the optimal sinter temperature because the pellet of the sintered sample at 700 °C was deformed. The temperature appears to be too high, possibly beyond the melting point of the material. The percentage of impurity phases is too high for further investigations, hence the synthesis has to further refined, for example, by a longer dwelling time in the future.

NFeL

The measured XRD patterns in Figure 24 show a comparison of NFeL sintered within a broad range of temperatures. All samples were mechanically milled before pressing into pellets and sintered for 15 h. During the reproduction of already existing methods (see Chapter 6.1.1) a successful synthesis was achieved with a high amount of impurities. For this chemical composition a DTA analysis is reported in the literature [20], where the melting point was observed at 645 °C. The sinter temperature should be below the melting point of the material. For every temperature the fluoride garnet structure (NFeL) can be observed. However, two impurity phases are detected as well LiF and Na_3FeF_6. The smallest amount of impurity phases contains the sample sintered at 500 °C. Nevertheless, the impurity phases are detectable, therefore the dwelling time could be not sufficient for a homogeneous diffusion.

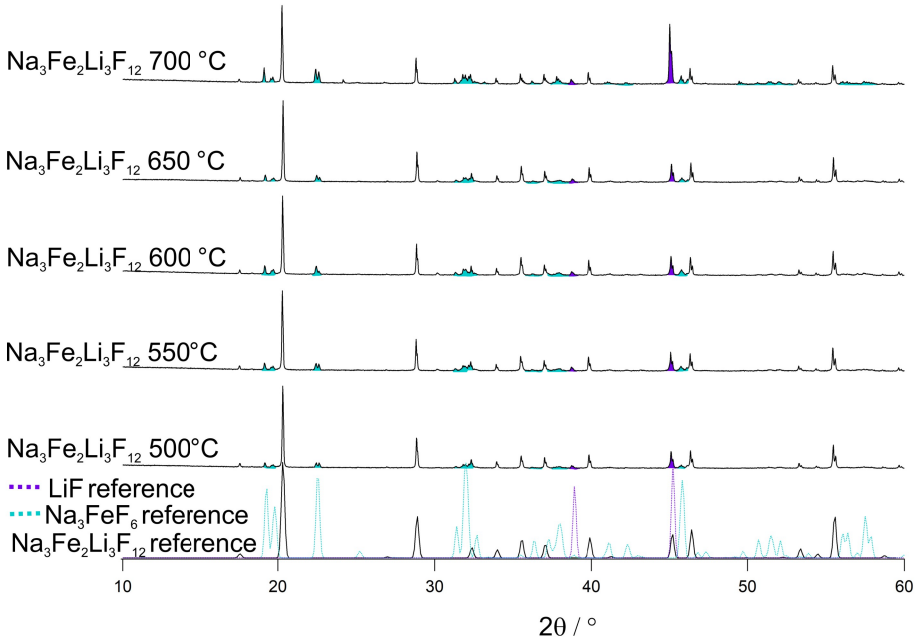

Figure 24.: NFeL, milled, dwelling time: 15 h, T = 500 °C - 700 °C [7]

Prior to this thesis Martin Philipp reproduced a fluid synthesis reported in the literature [20], with a range of different chemical compositions. The only fluoride garnet that was obtained purer with the fluid synthesis then during this thesis with the solid state synthesis was NFeL [28].

NMnL

Figure 25 displays a comparison of the XRD patterns with the chemical composition of NMnL sintered within a temperature range of 500 °C to 750 °C. All samples were mechanically milled before pressing into pellets and sintered for 15 h. During the reproduction of already existing methods (see Chapter 6.1.1) the synthesis showed no success. This chemical composition was published one time by Langley and Sturgeon [13]. They found in their experiment one impurity phase, a unidentified tetragonal phase (a = 5.63 Å, c = 4.12 Å) with a sinter temperature of 800 °C. They reported just one successful attempt. When comparing the patterns of the different temperatures in Figure 25 non of the samples contain the garnet structure that was calculated with VESTA. The found phases in the XRD pattern are LiF and $NaMnF_3$. Therefore no successful synthesis could be performed.

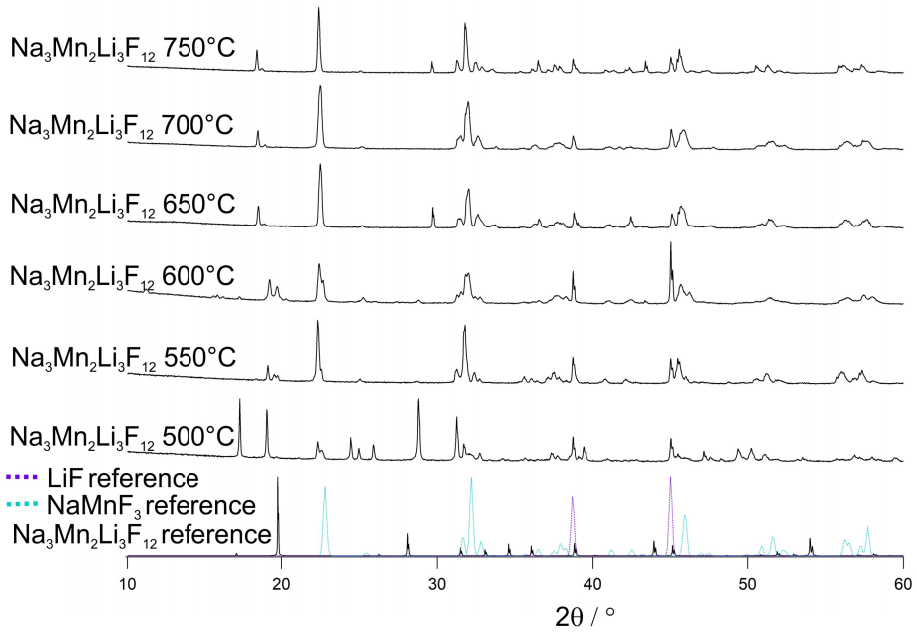

Figure 25.: NMnL, milled, dwelling time: 15 h, T = 500 °C and 750 °C [7]

6.2.2. Electrolyte Material

In the following section the future electrolyte materials are discussed. The resulting materials are described by XRD, SEM and EDX.

NAIL

The XRD pattern shown in Figure 26 compares two samples sintered at 600 °C for 15 h with a chemical composition of NAlL. The impact of an additional milling step before pressing the pellets is demonstrated. The milled samples show smaller reflections for the impurity phases. These phases can be identified as Na_3AlF_6 and LiF. The remains of these phases are probably a result of insufficient blending or dwelling time. The second sample in Figure 26 was not milled before pressing, therefore the particles of the reactants were bigger causing a lower reactive surface resulting in a higher amount of impurities. This chemical composition was previously only synthetically produced by a fluid synthesis.

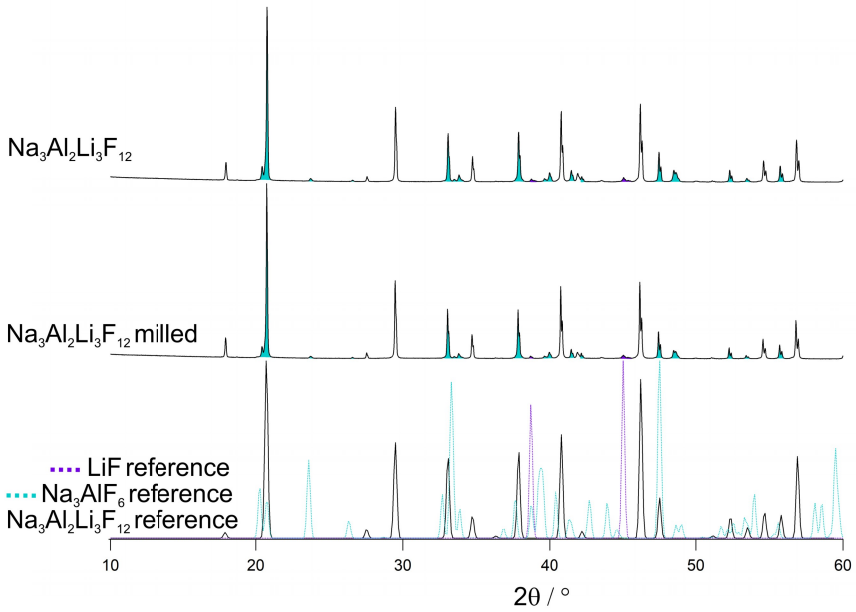

Figure 26.: XRD-pattern, NAlL milled and unmilled, T = 600 °C, dwelling time = 15 h [7]

The measured XRD patterns in Figure 27 show a comparison of NAlL sintered between 500 °C and 700 °C. All samples were mechanically milled before pressing into pellets and sintered for 15 h. For NAlL a DTA analysis is reported in the literature [20], where the melting point was observed at 695 °C. As previously mentioned the sinter temperature should be below the melting point of the material. Therefore, an adequate range of temperatures was chosen.

In all samples the reflections for Cryolithionite can be identified, nonetheless two additional phases can be detected, LiF and Na_3AlF_6. The XRD pattern of the sample sintered with 600 °C shows the smallest amount of impurity phases. This temperature is below the melting point and the pellet form is not lost during the synthesis. However, the conditions are still not optimal.

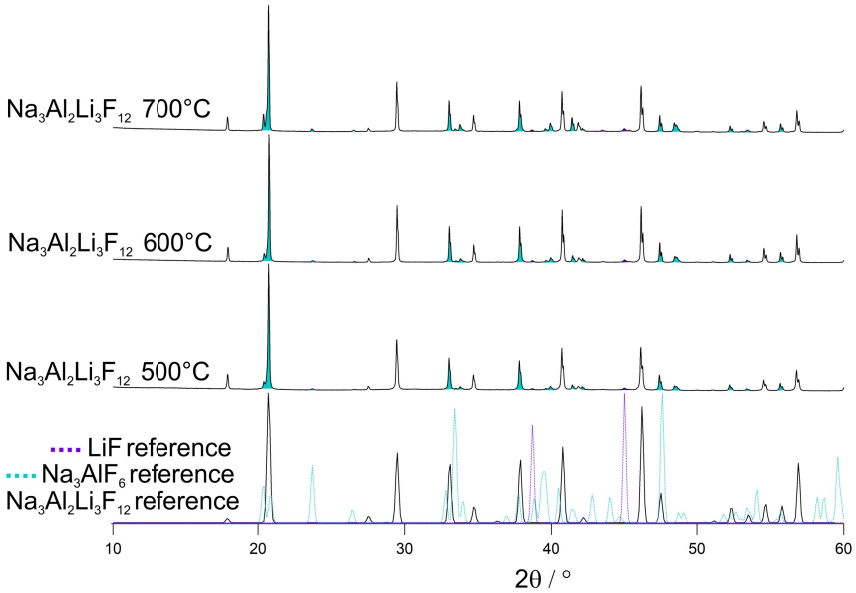

Figure 27.: NAlL, milled, dwelling time: 15 h, T = 600 °C - 700 °C [7]

Figure 28 shows the XRD patterns of three NAlL. The sinter temperature was 600 °C and the sinter time 15 hours for all samples. The reactants were ball milled before pressing into pellets. For this experiment three Cu- tubes were prepared with increasing amount of pellets. The increase in reactants in the sample holder during the sinter process should create a more homogeneous atmosphere and consequently less LiF would vaporize. With this technique a decrease in impurity phases was expected. However, the XRD-analysis showed no change in any of the samples (see Figure 28).

To further improve the purity of the sample, a second sinter step was used. The measured XRD pattern of NAlL sintered at 600 °C for 15 h with a ball milling step before pressing into pellets indicates that the impurity phases increase with the second sinter step. The sample was opened at room atmosphere in between the sinter steps, grained and analysed. The increase of impurities could be caused by a reaction with the atmosphere of remaining impurities and reactants after the first sinter steps. On the other hand could the increase of

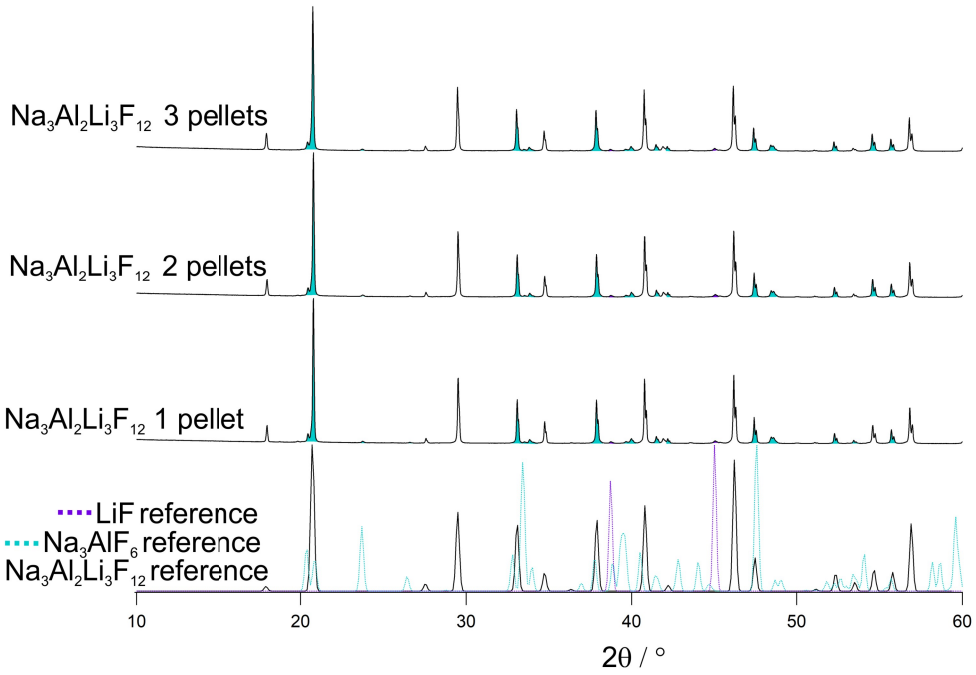

Figure 28.: XRD-pattern of multiple NAlL pellets in Cu-tube, T = 600 °C, dwelling time = 15 h [7]

impurities also be caused by decomposition. However, only the already existing impurities increase during the second sinter step. No additional phases are found.

NAlL has a very low Li-ion conductivity. To increase this property, the material NAlL is doped with divalent chemicals, MgF_2 and CaF_2 (Equation 5.2). Figure 30 compares the XRD pattern of the two doped samples with the undoped sample. All samples were ball milled, pressed into pellets and sintered at 600 °C for 15 h. For each sample the garnet structure is detected, nevertheless, two impurity phases are found, Na_3AlF_6 and LiF. When comparing the undoped sample with the MgF_2 doped sample, the impurity phases increase slightly. Nonetheless there is no additional phase of Mg detected. It is assumed that the material is build into the structure. The XRD pattern of the Ca doped samples shows reflections of an additional phase which can be identified as CaF_2. Thus, CaF_2 is not incorporated into the garnet structure due to a too big ion radius of Ca^{2+}.

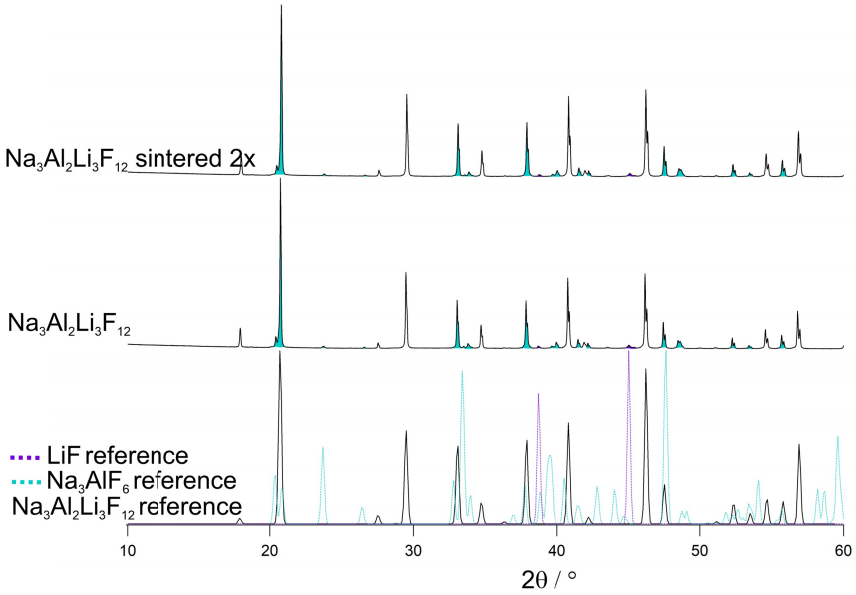

Figure 29.: XRD-pattern of NAlL samples with multiple sinter steps, T = 600 °C, dwelling time = 15 h [7]

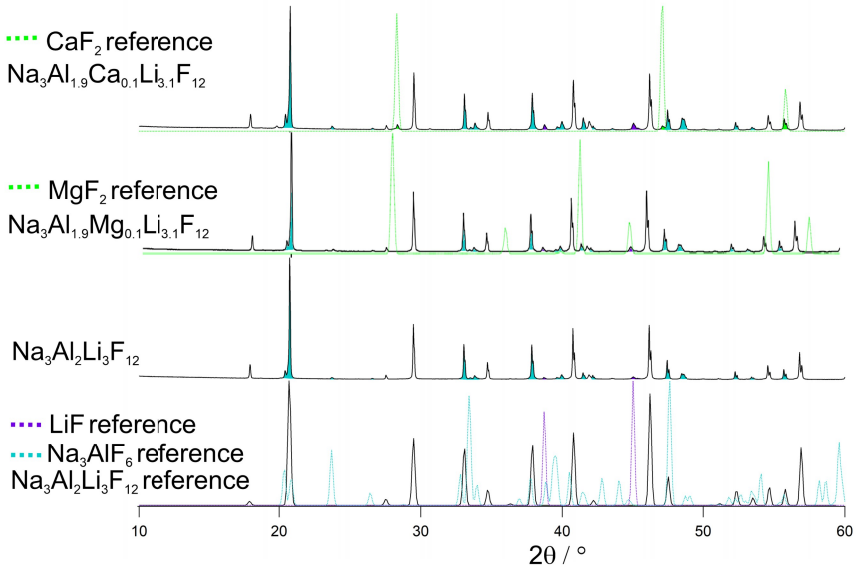

Figure 30.: XRD-pattern of NAlL CaF_2/MgF_2 doped samples[7]

NInL

Figure 31 shows two samples sintered at 600 °C for 15 h with a chemical composition of NInL. The impact of an additional milling step before pressing the pellets is visible. The XRD pattern of the milled sample shows a small amount of impurity phases. These impurity phases can be identified similar to previous chemical compositions as Cryolite where M = In and LiF. Nevertheless, one additional phase is detected, $NaInF_6$. The pattern for this phase ($NaInF_6$) was artificially calculated with VESTA. Theoretically, this chemical composition can not exist due to the oxidation state of In^{3+}. However, through defects in the crystal structure the diffraction pattern could appear as such. These impurity phases could be caused by insufficient amount of NaF and LiF in the sample. The second sample in Figure 31 was not milled before pressing therefore the particles of the reactants were bigger and the blending was less homogeneous leading to a higher amount of impurity phases.

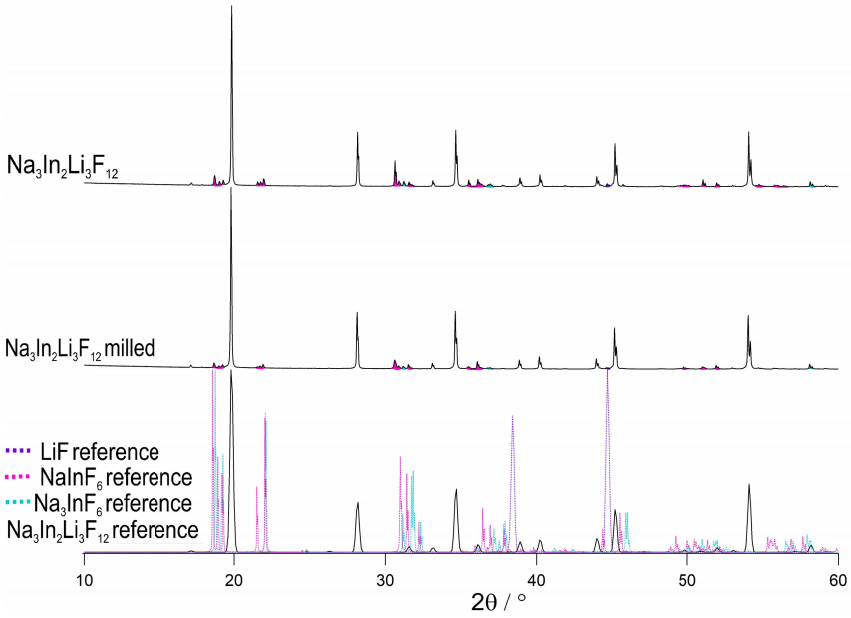

Figure 31.: XRD-pattern, NInL milled and unmilled, T = 600 °C, dwelling time = 15 h [7]

Figure 32 displays a comparison of the XRD patterns with the chemical composition of NInL sintered within a temperature range of 500 °C to 700 °C. All samples were mechanically milled before pressing into pellets and sintered for 15 h. When comparing the patterns of the different temperatures in Figure 32 all contain Cryolithionite with the trivalent cation In. For each sample the same impurity phases are found, $NaInF_6$, LiF and Na_3InF_6. However, the XRD pattern with the smallest amount of impurities is detected for the sample

sintered at 600 °C.

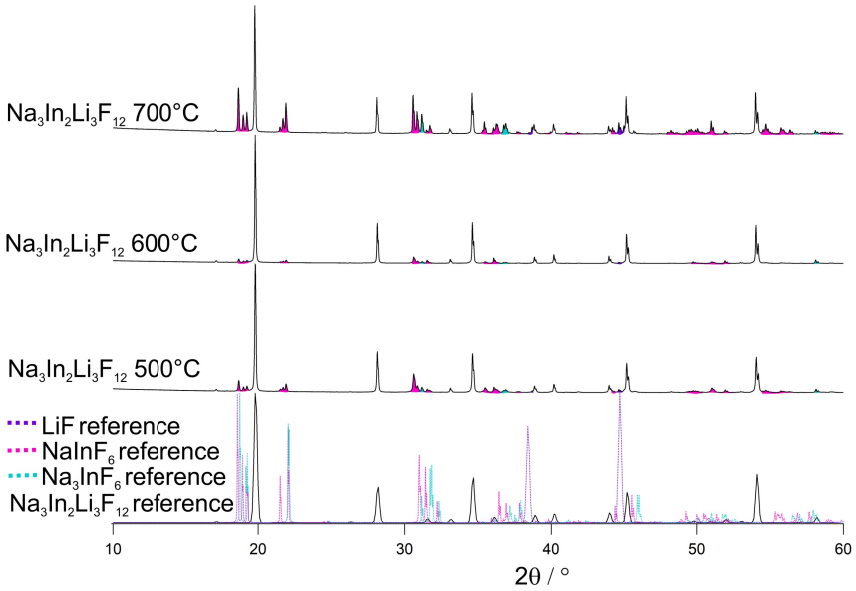

Figure 32.: NInL, milled, dwelling time: 15 h, T = 500 °C - 700 °C [7]

In Figure 33 images of NInL pellets after the solid state synthesis at 500 °C, 600 °C and 700 °C for 15 h. The sample sintered at 500 °C and 600 °C kept their form, but a shrinkage of the pellet is observed. The sample sintered at a higher temperature (700 °C) lost the pellet form during the synthesis indicating a too high sinter temperature. All samples had a dark outer layer and the color of the garnet material was grey.

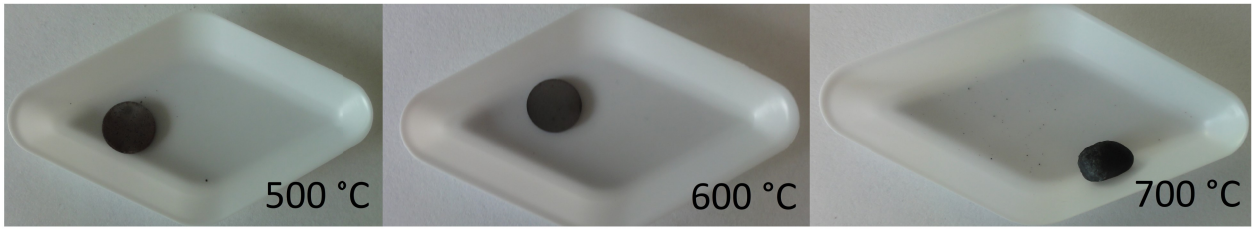

Figure 33.: image of samples with the chemical composition of NInL and dwelling time of 15 h, left sinter temperature 500 °C, middle sinter temperature 600 °C, right sinter temperature 700 °C [7]

The samples seen in Figure 34 were prepared with two sinter steps. All samples were ball milled, pressed into pellets and sintered for 15 h at 600 °C. After grinding the sintered material, half of the sample was taken outside the GB for XRD-analysis. After the analysis both

samples were pressed into pellets and sintered again for 15 h at a temperature of 600 °C. When comparing the sample with one sinter step with the two other samples the best results where achieved with one sinter step. For all samples the same impurity phases are found, Na_3InF_6, $NaInF_6$ and LiF. Nevertheless, through the implementation of the second sinter step the amount of impurity phases increases as well, especially for the sample that was kept under room atmosphere in between the sinter steps. On the other hand could the increase of impurities also be caused by decomposition. On the other hand, the XRD results show only an increase of the already found impurity phases and no appearance of additional new phases due to possible interaction with, for example, oxygen. Another explanation would be decomposition.

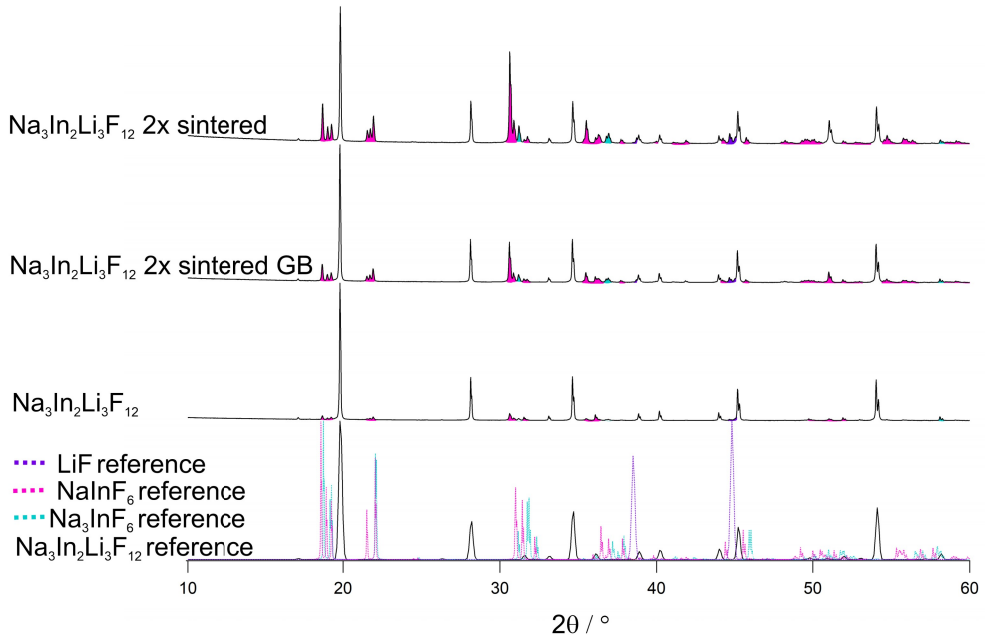

Figure 34.: NInL comparison of one sinter step and two sinter steps, sinter time 15 h and sinter temperature 600 °C. One sample stayed in the GB between sinter steps, the other one was opened at room atmosphere [7]

To increase the Li-ion conductivity of the material, NInL is doped with a divalent material, CaF_2 (Equation 5.2). Figure 35 shows the XRD patterns of NInL doped with an increasing amount of CaF_2 (x= 0 to x= 0.3). All samples were ball milled, pressed into pellets and sintered at 600 °C for 15 h. For each sample the garnet structure is detected, nevertheless three impurity phases are found for every sample Na_3InF_6, $NaInF_6$ and LiF. When comparing the sample x = 0 with the x > 0 sample, the impurity phases increase slightly and

reflections of a additional phase are detected, CaF_2. Therefore, the doping material does not get incorporated in the garnet structure which is caused by a too big ion radius of Ca^{2+}.

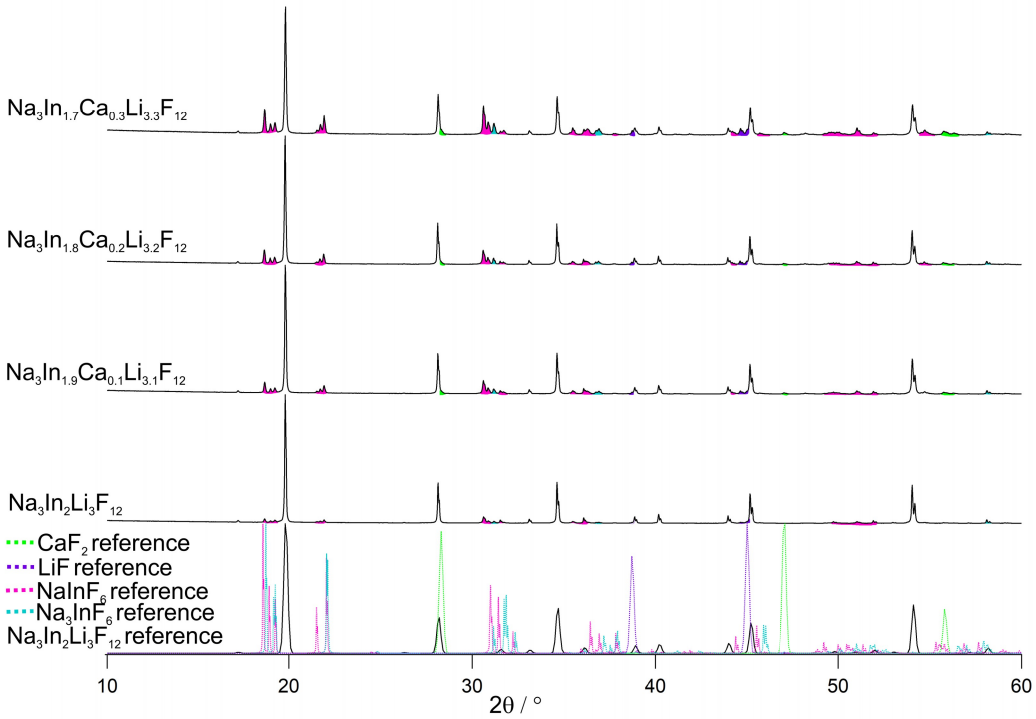

Figure 35.: acXRD-pattern of a NInL sample doped with CaF_2 (x = 0 to x = 0.3), dwelling time = 15 h, T = 600 °C [7]

Figure 36 shows a SEM image generated with a SE signal of NInL doped with x = 0.1 Ca. SE imaging shows the topographic contrast of a sample. The image was taken with a high magnitude. The material is polycrystalline with a very small grain size.

A second image of this sample was taken, see Figure 37. Equal to the first image SE were used for imaging. Nevertheless, a lower magnification was utilised. The indicated spots in Figure 37 were investigated by an EDX analysis. In Table 2 the results are displayed. For each indicated spot the chemical composition was investigated. Ca was not found in any of them. Therefore, the element is not incorporated in the crystal structure, emphasized both by the EDX and XRD analysis results.

To further improve the purity, of the samples a second sinter step was introduced. All samples have the chemical composition of NInL with x = 0.1 Ca. The samples were ball milled,

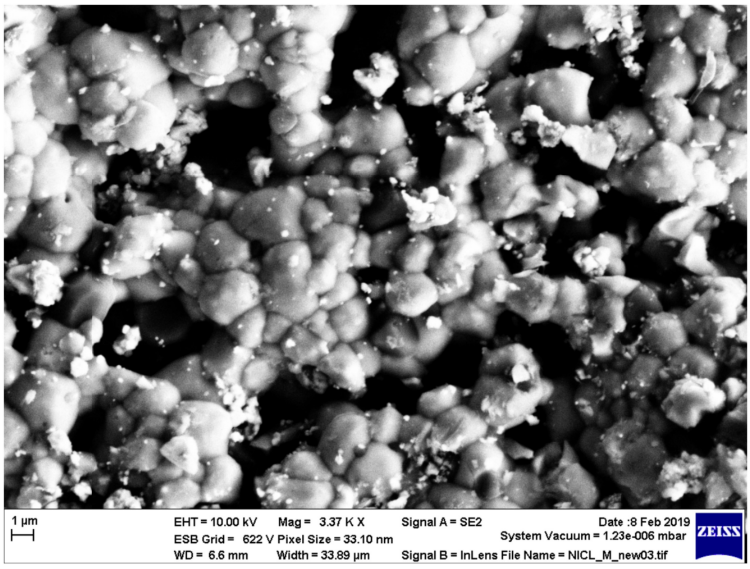

Figure 36.: SEM image of NInL doped with 0.1 CaF_2, dwelling time = 15 h, T = 600 °C

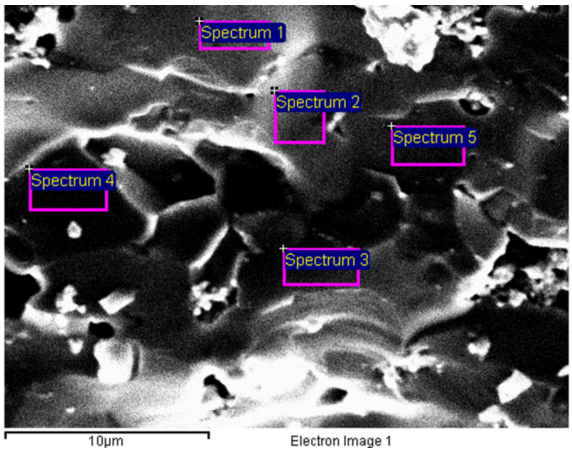

Figure 37.: SEM image of a NInL pellet doped with 0.1 CaF_2, dwelling time = 15 h. The EDX spectra seen in Table 2 were taken from the indicated areas.

Table 2.: EDX Spectra of NInL doped with 0.1 CaF_2

Spectrum	F	Na	Ca	In
Spectrum 1	56.64	10.43	0	32.93
Spectrum 2	58.86	10.79	0	30.35
Spectrum 3	53.04	9.90	0	37.06
Spectrum 4	50.40	9.20	0	40.40
Spectrum 5	52.05	9.93	0	38.02
Mean	54.20	10.05	0	35.75
Std. deviation	3.47	0.60	0	4.05
Max.	58.86	10.79	0	40.40
Min.	50.40	9.20	0	30.35

pressed into pellets and sintered for 15 h at 600 °C. After grinding the sintered material, half of the sample was taken outside the GB for XRD-analysis. Subsequently both samples were pressed into pellets and sintered again for 15 h at a temperature of 600 °C. When comparing the sample sintered once with the two other samples, the best results where achieved with a one step synthesis similar to the previously discussed undoped NInL sample. For all samples the cubic garnet structure and impurity phases are detected, Na_3InF_6, $NaInF_6$, CaF_2 and LiF. Nevertheless, through the implementation of the second sinter step the amount of impurity phases increases, especially for the sample that was kept under room atmosphere in between the sinter steps. On the other hand, the XRD results show only an increase of the already found impurity phases and no appearance of additional new phases from interaction with other elements, for example, oxygen. This could also be caused by decomposition.

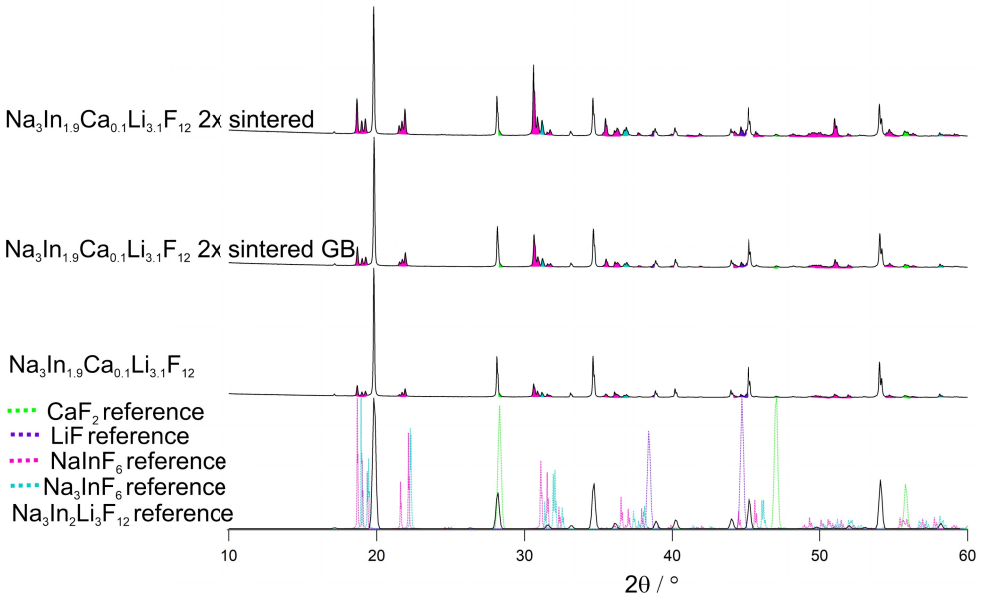

Figure 38.: XRD-pattern of a NInL samples doped with CaF_2 with multiple sinter steps, T = 600 °C, dwelling time = 15 h [7]

The measured XRD patterns of NInL doped with Mg (x=0 to x= 0.2), ball milled, sintered at 600 °C for 15 h indicate an increase of impurity phases with increasing Mg content. However, all samples exhibit the cubic garnet structure. The identified impurity phases are LiF, $NaInF_6$ and Na_3InF_6 similar to the other NInL samples seen above. Nonetheless, reflections for MgF_2 are not detected. This leads to the assumption that Mg gets integrated into the cubic crystal structure of the garnet.

A SEM image generated with SE of the NInL doped with x= 0.1 Mg pellet is shown in Figure 40. The sample is polycrystalline equal to the Ca doped sample discussed previously. However, the grain size is bigger.

In Figure 41 a SEM image of the same sample is shown with a lower magnification. The indicated spots show where the chemical composition was measured with an EDX analysis. Results are shown in Table 3. For every measurement all elements of the garnet are found. These findings correspond to the XRD analysis of this sample. Mg seem to be included into the garnet structure.

To further investigate the outcome of a synthesis with two sinter steps, NInL with x = 0.1 Mg was sintered twice as well. The samples were ball milled, pressed into pellets and sintered

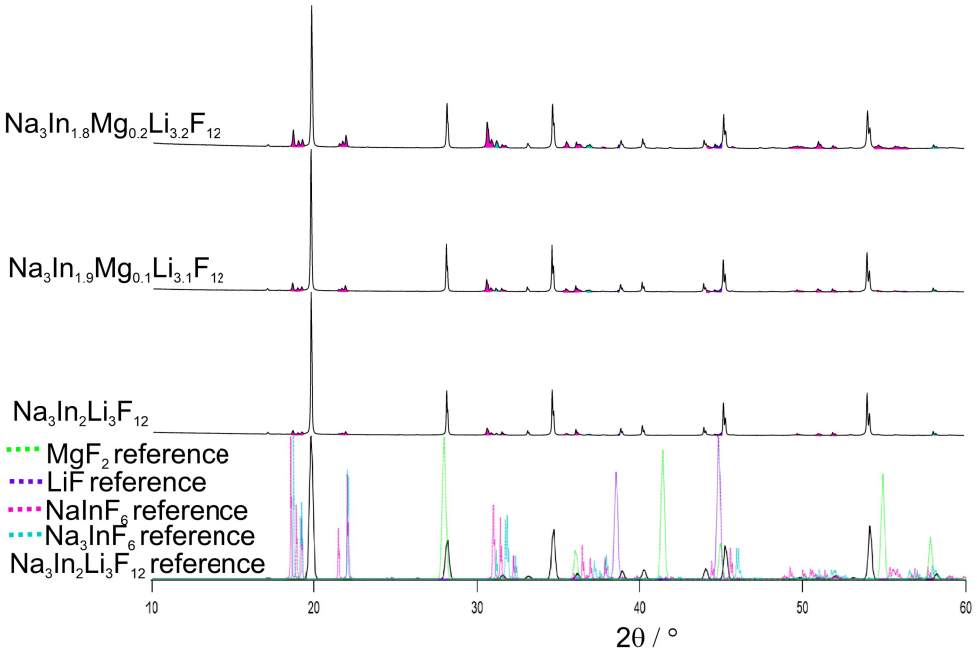

Figure 39.: acXRD-pattern of a NInL sample doped with MgF_2 (x = 0 to x = 0.2), dwelling time = 15 h, T = 600 °C [7]

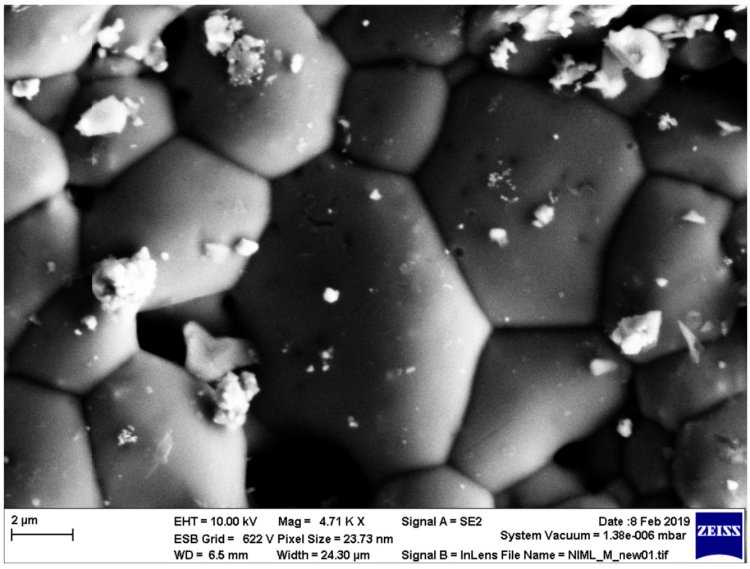

Figure 40.: SEM image of NInL doped with 0.1 MgF_2, dwelling time = 15 h, T = 600 °C

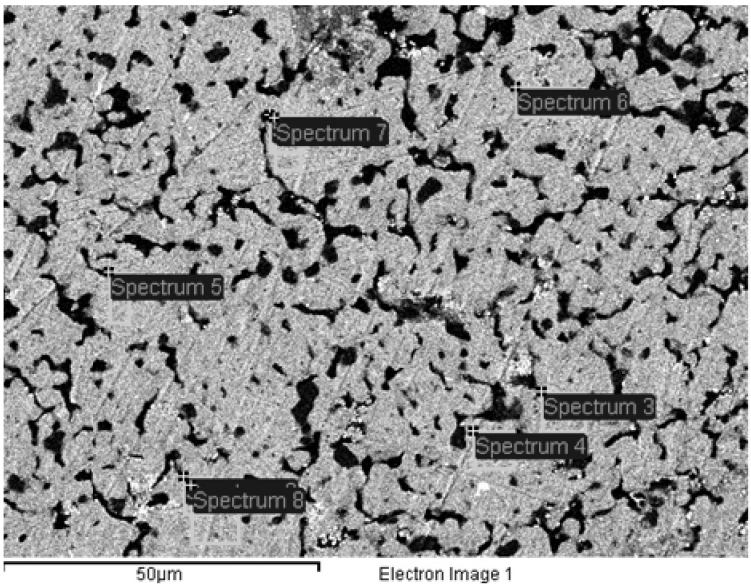

Figure 41.: SEM image of a NInL pellet doped with 0.1 MgF_2, dwelling time = 15 h. The EDX spectra seen in Table 3 were taken from the indicated areas.

Table 3.: EDX Spectra of NInL doped with 0.1 MgF_2

Spectrum	F	Na	Mg	In
Spectrum 1	53.10	10.72	0.41	35.77
Spectrum 2	52.65	10.88	0.68	35.78
Spectrum 3	52.26	11.85	0.15	35.74
Spectrum 4	52.49	10.66	0.21	36.64
Spectrum 5	52.84	10.75	0.20	36.21
Spectrum 6	52.94	10.47	0.26	36.32
Spectrum 7	52.53	11.21	0.45	35.82
Spectrum 8	52.08	11.33	0.42	36.17
Mean	52.61	10.98	0.35	36.06
Std. deviation	0.34	0.45	0.18	0.33
Max.	53.10	11.85	0.68	36.64
Min.	52.08	10.47	0.15	35.74

for 15 h at 600 °C. After grinding the sintered material, half of the sample was taken outside the GB for XRD-analysis. Afterwards both samples were pressed into pellets and sintered again for 15 h at a temperature of 600 °C. When comparing the sample sintered once with the two other samples, the best results where achieved with a one step synthesis similar to the previously discussed undoped and doped NInL sample. For all samples the cubic garnet structure and the same impurity phases are detected, Na_3InF_6, $NaInF_6$ and LiF. Nevertheless, through the implementation of the second sinter step the amount of impurity phases increases, especially for the sample that was kept under room atmosphere in between the sinter steps. On the other hand, the XRD results show only an increase of the already found impurity phases and no appearance of additional new phases from interaction with other elements, for example, oxygen. This could also be caused by decomposition. Each chemical composition that was sintered with two sinter steps show the same result.

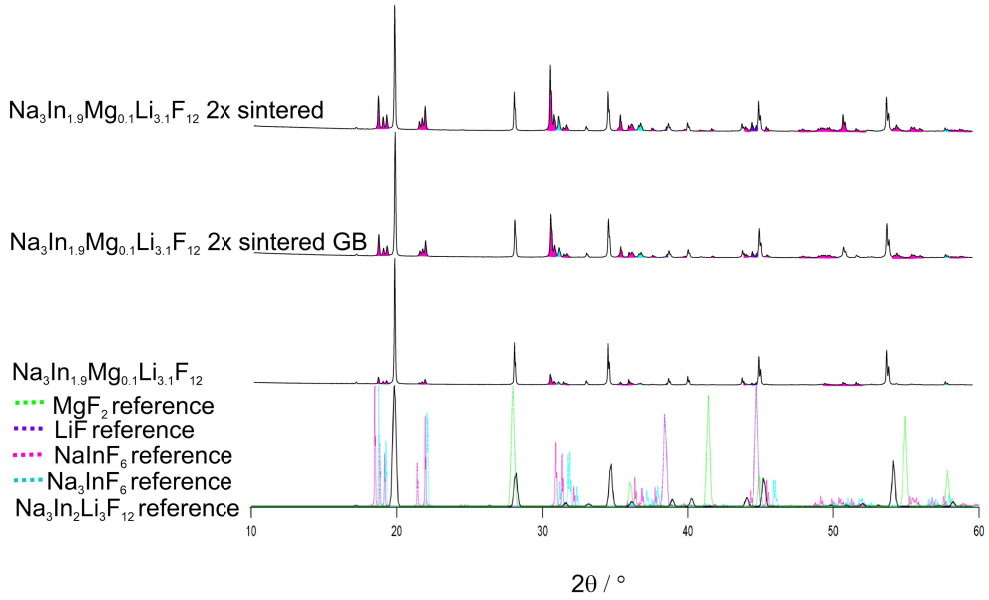

Figure 42.: XRD-pattern of a NInL samples doped with MgF_2 with multiple sinter steps, T = 600 °C, dwelling time = 15 h [7]

Figure 43 shows a NInL sample doped with x = 0.2 Mg sintered in a Ni-tube compared to a doped and undoped sample sintered in a Cu-tube. The samples were ball milled, pressed into pellets and sintered for 15 h at 600 °C. The diameter of the Ni-tube is smaller (8 mm) therefore smaller pellets (5 mm) had to be prepared. Each sample shows the cubic garnet structure and the same impurities , Na_3InF_6, $NaInF_6$ and LiF_2. However, the intensity of the impurity phases vary. The sample sintered in the Ni-tube shows a smaller amount

of impurity phases. Interactions with the crucible can not be observed for any of the samples.

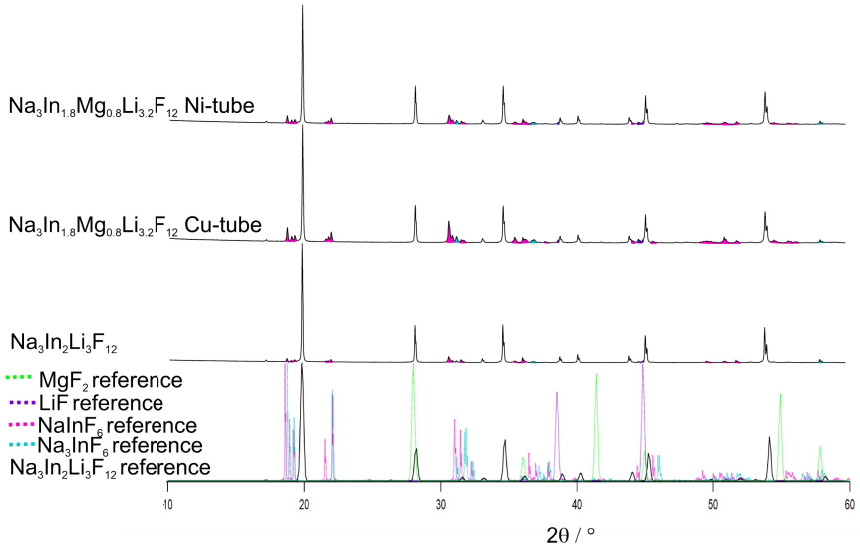

Figure 43.: XRD-pattern comparing NInL samples doped with MgF_2 sintered in different crucibles (Ni-tube/Cu-tube), dwelling time = 15 h, T = 600 °C [7]

To increase the Li-ion content to potentially increase the Li-ion conductivity of NInL, another divalent element was used, CuF_2 (compare Equation 5.2). Figure 44 shows the XRD patterns of NInL doped with x = 0.1 Cu and as a comparison an undoped NInL sample. Both samples were ball milled, pressed into pellets and sintered at 600 °C for 15 h. Three impurity phases are detected for both samples Na_3InF_6, $NaInF_6$ and LiF. When comparing the x = 0 sample with the x = 0.1 sample, the impurity phases increase slightly. However, in comparison to the Mg and Ca doped NInL the increase is small. Similar to the Mg doped samples no additional phase for the doping material is detected. Thus, Cu gets included into the garnet structure.

In Figure 45 the XRD-pattern of the 0.1 Zn doped NInL sample sintered in a Ni-tube is compared to an undoped NInL sample sintered in a Cu-tube. The samples were ball milled, pressed into pellets and sintered at 600 °C for 15 h. The cubic garnet structure can be detected for both samples, however similar to previous NInL samples three impurity phases are detected, Na_3InF_6, $NaInF_6$ and LiF. Nonetheless, the amount of impurity phases for the ZnF_2 doped material was small in comparison to other previously investigated doped samples. No additional phase of ZnF_2 was detected in the XRD-pattern and the ion radius is similar to Mg and Cu. Regarding these results a successful incorporation of the doping

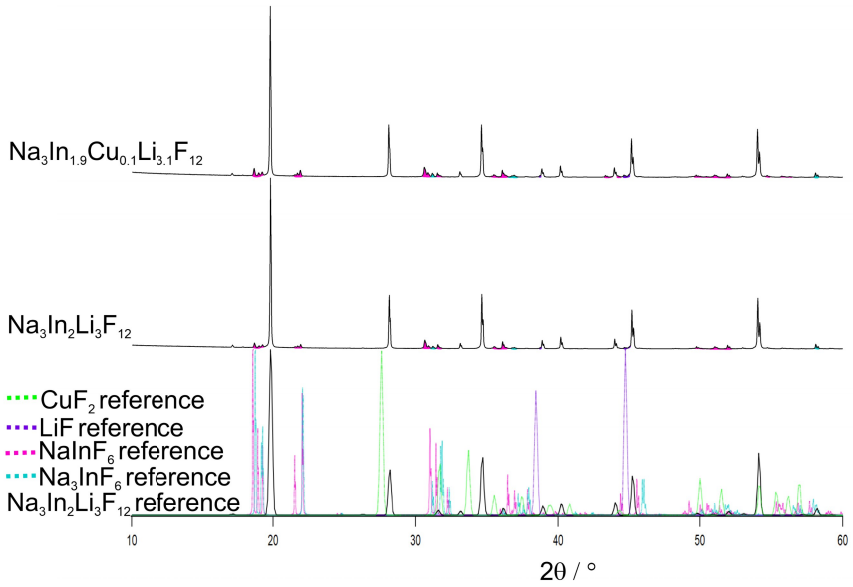

Figure 44.: XRD pattern of NInL doped with 0.1 CuF_2, dwelling time = 15 h, T = 600 °C [7]

material into the garnet structure can be assumed. The LiF phase is equal for the doped and undoped sample. Therefore the Li^+ per formula should increase as predicted.

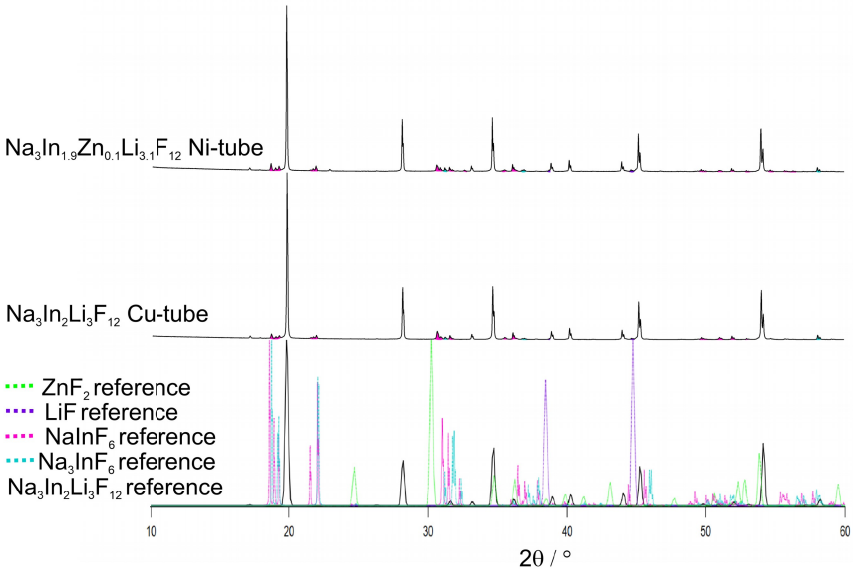

Figure 45.: XRD pattern of NInL doped with 0.1 ZnF_2, dwelling time = 15 h, T = 600 °C, crucible = Ni-tube [7]

NGaL

Figure 46 displays a comparison of the XRD patterns with the chemical composition of NGaL sintered within a temperature range of 550 °C to 750 °C. All samples were mechanically milled before pressing into pellets and sintered for 15 h. All samples show reflections for the cubic garnet structure. However, two impurity phases are found for each sample as well LiF and Cryolite with the trivalent cation Ga^{3+}. The sample sintered at 550 °C shows the smallest amount of impurities.

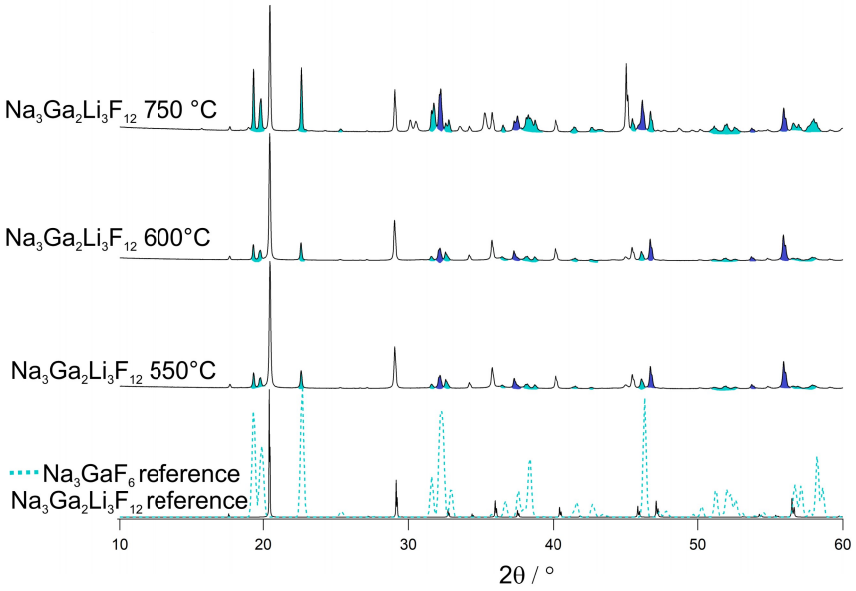

Figure 46.: NGaL, milled, dwelling time: 15 h, T = 550 °C - 750 °C [7]

One issue concerning the formation of impurities is an insufficient amount of LiF due to LiF interacting with the Cu-tube or evaporation of the same. Therefore, one experiment was conducted with different quantities of additional LiF. The NGaL samples were doped with x = 0.1 Mg. All samples were mechanically milled and additional LiF was added before pressing into pellets and sintered for 15 h at 550 °C. For one sample the pellet with the original composition was bedded into lose LiF powder. The amount of extra LiF varied for each sample. For every sample the reflections of the cubic garnet structure are detected. Additionally, LiF and Na_3GaF_6 can be observed. No additional phase for MgF_2 was found. This indicates that the doping could have been successful, although an insufficient number of samples were prepared for a reliable statement. For the samples with 20 %, 10 % and extra powder of LiF the intensity of the impurity phases are comparable but a small increase of

the LiF phase is seen in comparison to the samples where no LiF was added. The sample with 100 % more LiF shows a bigger increase of the LiF phase.

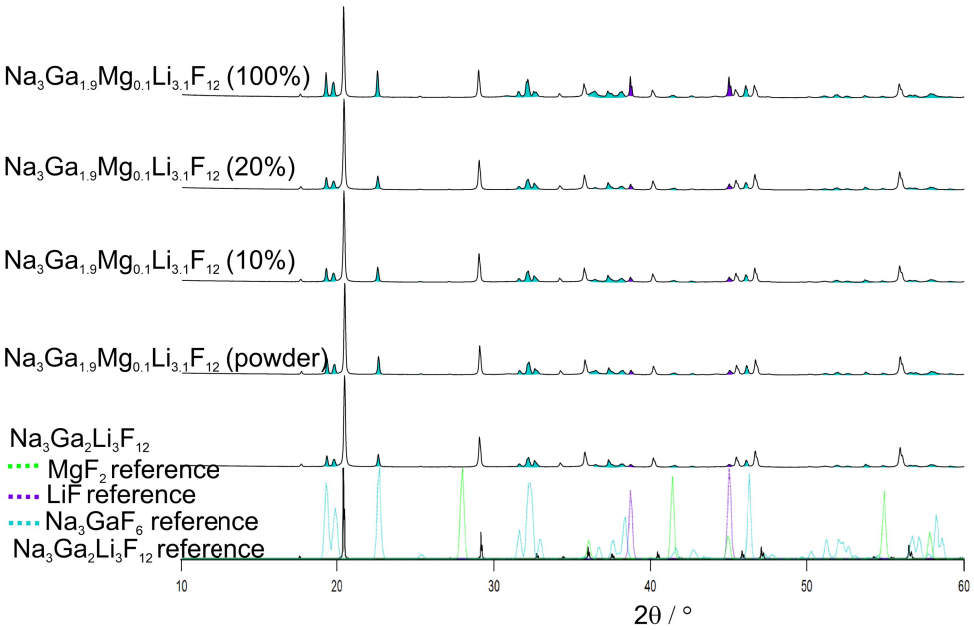

Figure 47.: XRD pattern of NGaL doped with 0.1 MgF_2 with additional LiF, dwelling time = 15 h, T = 550 °C [7]

The measured XRD pattern shown in Figure 48 of NGaL sintered at 550 °C for 15 h with a ball milling step before pressing into pellets indicates that the impurity phases increase with the second milling step. The sample was opened at room atmosphere in between the sinter steps and grained. The second sinter step was carried out at the same conditions. The increase of impurities could be caused by a reaction with the atmosphere of remaining impurities and reactants after the first sinter step. However, no additional impurity phases which would suggest an interaction with the room atmosphere are detected. On the other hand could the increase of impurities also be caused by decomposition. Another explanation could be decomposition. These findings are comparable with previously discussed results.

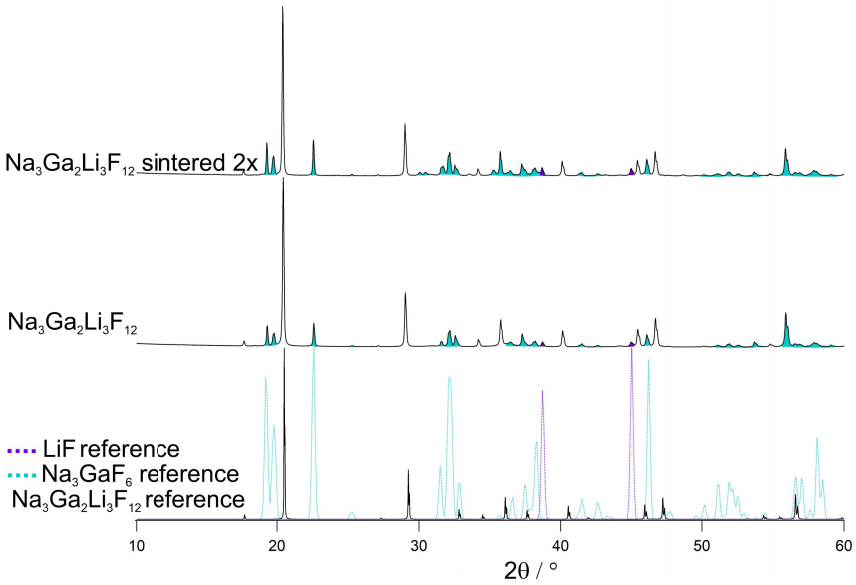

Figure 48.: XRD-pattern of a NGaL samples with multiple sinter steps, T = 550 °C, dwelling time = 15 h [7]

6.3. Lattice Constant

The most promising XRD results were used to calculate the lattice constant for each chemical composition.

Table 4 shows all from the XRD pattern calculated lattice constants compared to the ion radius of the trivalent cation. The lattice constant of the chemical compositions experiences a shift depending on the element at the M position ($Na_3M_2Li_3F_6$). The shifts can be clearly observed in Table 4, with growing ion radius the lattice constant increases. In case of the doped material the same principle should apply when N ($Na_3[M_{2x-y}N_y]Li_{3+y}F_{12}$) changes or/and increases. However, the additional LiF could also change the lattice constant. The lattice constant of the resulting doped material vary within the error limit, therefore no accurate determination can be made.

The lattice constant of the synthesized NAlL sample is 12.1215 ± 0.0002 Å. When comparing it to the value found for the naturally occurring Cryolithionite, 12.122 ± 0.002 Å, it lies within the error limit [18]. The value found by Takeda et al. 1977 from a sample synthesised by a fluid synthesis is 12.119(4) Å which is significantly lower [20].

The obtained lattice constant for NTiL is 12.4855 ± 0.0001 Å. Langley et al. 1978 found

Table 4.: Lattice Constant

Garnet	Grid Parameter/Å	Standard Derivation/Å	Ion Radius of M/Å
NAlL	12.1215	0.0003	0.5
NAlL N = Mg	12.1274	0.0004	
NAlL N = Ca	12.1263	0.0004	
NCrL	12.3307	0.0001	0.62
NGaL	12.3070	0.0004	0.62
NVL	12.4020	0.0004	0.64
NFeL	12.4002	0.0002	0.647
NTiL	12.4855	0.0001	0.67
NInL N=Mg 0.2	12.6970	0.0003	
NInL N=Mg 0.2,Ni	12.6971	0.0003	
NInL N=Mg 0.1	12.6940	0.0002	
NInL N=Cu 0.1	12.6960	0.0002	
NInL N=Zn 0.1	12.6958	0.0002	
NInL	12.6979	0.0004	0.92
NInL N=Ca 0.1	12.6949	0.0004	
NInL N=Ca 0.2	12.6930	0.0003	
NInL N=Ca 0.3	12.6935	0.0004	

with their solid state method a lattice constant of 12.495 ± 0.011 Å for the resulting material, the value lies within the error limit [29]. The lattice constant detected for NVL (12.4020 ± 0.0004 Å) is significantly lower than the one found by Langley et al. 1978 (12.434 ± 0.006 Å)[29].

The lattice content of the synthesised NCrL sample is 12.3307 ± 0.0004 Å. Takeda et al. 1977 found for this composition a constant of 12.334(4) Å and Langley et al. 1978 a value of 12.340 ± 0.006 Å. Both are significantly higher [20] [29] than the constant calculated during this work.

In the paper of Massa et al. the lattice constant for the synthesized fluoride garnet with the trivalent cation Fe^{3+} is 12.387(2) Å [21]. Two additional values can be found in literature for this constant, 12.404 ± 0.0005 Å by Langley et al. 1978 and 12.407(2) Å by Takeda et al. 1977 [20] [29]. The obtained lattice constant during this experiment is 12.4002 ± 0.0002 Å which is close to two of the three found values in literature.

7. Summary and Outlook

During the elaboration of this thesis a solid state synthesis of fluoride garnets was refined and optimized. In a first step the solid state synthesis found in the literature were reproduced. The results were characterised with a XRD analysis. Based on the first findings the impact of particle size, chemical composition, sinter temperature as well as the amount of sinter steps was analysed for each chemical composition. The resulting materials were characterized with XRD, SEM and EDX.

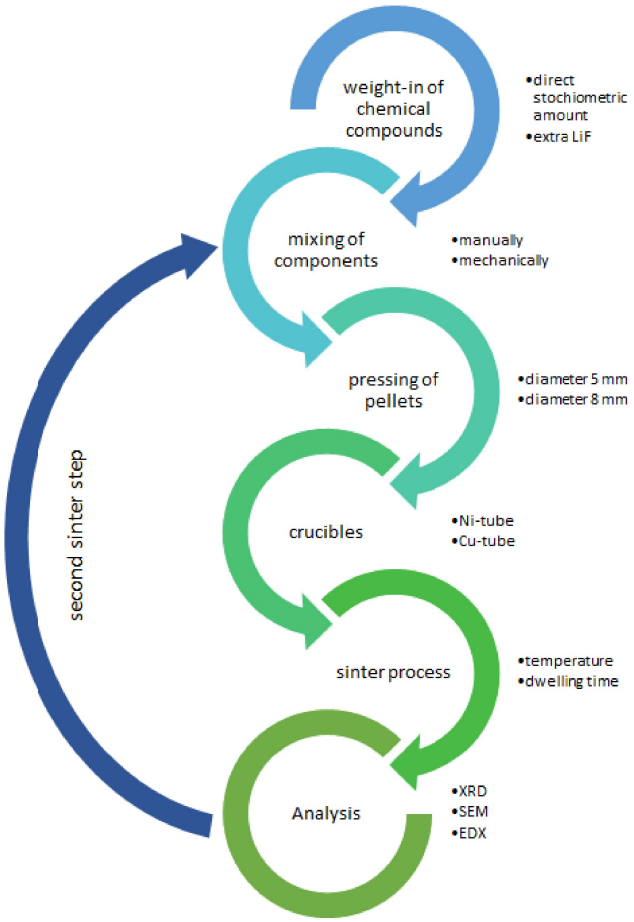

Figure 49.: Synthesis Process

The most successful results were found for samples with a dwelling time of 15 hours, and a milling process before pressing the pellets. The optimal sinter temperatures for each chemical composition can be found in Table 5. These temperatures are significantly lower then temperatures used in previous published solid state methods for fluoride garnets. The purity of their findings is not quantified in these publications, therefore a comparison is difficult.

Table 5.: Best Sinter Temperature for Fluoride Garnets

Garnet	Temperature/°C
NAlL	600
NInL	600
NGaL	500
NTiL	700
NCrL	600
NVL	550
NFeL	500

There are still challenges left. Owing to the results that were found during these experiments, a longer sinter time could further improve the purity of the samples. The impurity phases that are found in all samples after the sinter process are LiF and Na_3MF_6 which could mean that the dwelling time is too short, therefore the chemicals do not have enough time to react. Another issue is the interaction of the sample with the sample holder, the Cu-tube. In the XRD-patterns the interaction was only observed for NVL at the optimal sinter temperature. One possible solution is the replacement of Cu-tubes by Ni-tubes. Just a small amount of experiments were executed with Ni-tubes therefore no clear determination can be made about the interaction of the Ni-tube with the samples.

After optimizing the materials, electrochemical testing should be done. For example, impedance measurements to find the optimal amount of doping for electrolyte materials should be conducted. For the potential electrode material cyclic voltammetry (CV) and galvanostatic cycling (GCPL) measurements should be conducted. Especially interesting would be the discovery of high voltage cathode materials and high Li-ion conducting electrolyte materials.

Bibliography

[1] AADVIKPATEL: *Lithium Ion Battery: What Are The Types?* http://aadvikpatel.zohosites.com/blogs/post/Lithium-Ion-Battery-What-Are-The-Types. Version: Januar 2019

[2] DUDNEY, Nancy J. ; WEST, William C. ; NANDA, Jagjit: *Handbook of Solid State Batteries*. 2nd. WORLD SCIENTIFIC, 2015. http://dx.doi.org/10.1142/9487. http://dx.doi.org/10.1142/9487

[3] ZHENGCHENG ZHANG, Sheng Shui Z. (Hrsg.): *Rechargeable Batteries Materials, Technologies and New Trends*. Springer, 2015. – ISBN 978–3–319–15458–9

[4] REINHARD WAGNER, Georg A. Daniel Rettenwander R. Daniel Rettenwander: Lithium ion - conduction oxid garnets. In: *Highlights in Applied Mineralogy (pp. 3-22)* (2017). https://www.degruyter.com/view/books/9783110497342/9783110497342-001/9783110497342-001.xml

[5] SCOTT, Michael: *Cryolithionite R080051*. http://rruff.info/Cryolithionite. Version: November 2019

[6] COMMONSWIKI, Claudionico: *File:Electron Interaction with Matter.svg*. https://en.wikipedia.org/wiki/File:Electron_Interaction_with_Matter.svg. Version: Dezember 2013

[7] ; Fachinformationszentrum (FIZ) Karlsruhe und das National Institute of Standards and Technology, USA (Veranst.): *Inorganic Crystal Structure Database - ICSD*. https://icsd.fiz-karlsruhe.de/. Version: Dezember 2019

[8] LANGLEY, Richard H. ; STURGEON, George D.: Lattice parameters and ionic radii of the oxide and fluoride garnets. In: *Journal of Solid State Chemistry* 30 (1979), Nr. 1, 79 - 82. http://dx.doi.org/https://doi.org/10.1016/0022-4596(79)90132-4. – DOI https://doi.org/10.1016/0022–4596(79)90132–4. – ISSN 0022–4596

[9] Korthauer, Reiner: *Handbuch Lithium-Ionen-Batterien*. Springer, 2013. http://dx.doi.org/10.1007/978-3-642-30653-2. http://dx.doi.org/10.1007/978-3-642-30653-2. – ISBN 978–3–642–30652–5

[10] Zheng, Feng ; Kotobuki, Masashi ; Song, Shufeng ; Lai, Man O. ; Lu, Li: Review on solid electrolytes for all-solid-state lithium-ion batteries. In: *Journal of Power Sources* 389 (2018), 198 - 213. http://dx.doi.org/https://doi.org/10.1016/j.jpowsour.2018.04.022. – DOI https://doi.org/10.1016/j.jpowsour.2018.04.022. – ISSN 0378–7753

[11] Wagner, Reinhard ; Redhammer, Günther J. ; Rettenwander, Daniel ; Tippelt, Gerold ; Welzl, Andreas ; Taibl, Stefanie ; Fleig, Jürgen ; Franz, Alexandra ; Lottermoser, Werner ; Amthauer, Georg: Fast Li-Ion-Conducting Garnet-Related Li7-3xFexLa3Zr2O12 with Uncommon I4-3d Structure. In: *Chemistry of Materials* 28 (2016), 8, Nr. 16, S. 5943–5951. http://dx.doi.org/10.1021/acs.chemmater.6b02516. – DOI 10.1021/acs.chemmater.6b02516. – ISSN 0897–4756

[12] Thangadurai, Venkataraman ; Narayanan, Sumaletha ; Pinzaru, Dana: Garnet-type solid-state fast Li ion conductors for Li batteries: critical review. In: *Chem. Soc. Rev.* 43 (2014), 4714-4727. http://dx.doi.org/10.1039/C4CS00020J. – DOI 10.1039/C4CS00020J

[13] Langley, Richard H. ; Sturgeon, George D.: Synthesis of transition-metal fluoride garnets. In: *Journal of Fluorine Chemistry* 14 (1979), Nr. 1, 1 - 6. http://dx.doi.org/https://doi.org/10.1016/S0022-1139(00)82987-5. – DOI https://doi.org/10.1016/S0022–1139(00)82987–5. – ISSN 0022–1139

[14] Elektrochemie ; Hamann, Wolf Carl H. / V. Carl H. / Vielstich (Hrsg.): *Elektrochemie*. 4. WILEY-VCH, 2005. – ISBN 978–3–527–31068–5

[15] Florian Spieler, Kilian H.: *Der Lithium-Ionen-Akku*. http://daten.didaktikchemie.uni-bayreuth.de/umat/lithiumionenakku/lithiumionenakku.htm#Laden. Version: Juli 2018

[16] Kim, Joo G. ; Son, Byungrak ; Mukherjee, Santanu ; Schuppert, Nicholas ; Bates, Alex ; Kwon, Osung ; Choi, Moon J. ; Chung, Hyun Y. ; Park, Sam: A review of lithium and non-lithium based solid state batteries. In: *Journal of Power Sources* 282 (2015), 299 - 322. http://dx.doi.org/https://doi.org/10.1016/j.jpowsour.

2015.02.054. – DOI https://doi.org/10.1016/j.jpowsour.2015.02.054. – ISSN 0378–7753

[17] Callister, W.D. ; Rethwisch, D.G.: *Materials Science and Engineering: An Introduction, 8th Edition*. Wiley, 2009 https://books.google.at/books?id=OaIbAAAAQBAJ. – ISBN 9780470941669

[18] Geller, S.: Refinement of the Crystal Structure of Cryolithionite , Na3J[AI2](Lb)F12. In: *The American Mineralogist* 56 (1971), S. 18–23

[19] Naka, Shigeharu ; Takeda, Yasuo ; Sone, Masahiro ; Suwa, Yoshiko: SYNTHESIS OF THE FLUORIDE GARNETS Na3[M23+](Li3)F12 (M=Al, Cr, Fe). In: *Chemistry Letters* 4 (1975), Nr. 7, 653-654. http://dx.doi.org/10.1246/cl.1975.653. – DOI 10.1246/cl.1975.653

[20] Takeda, Y. ; Sone, M. ; Suwa, Y. ; Inagaki, M. ; Naka, S.: Synthesis of fluoride garnets Na3[M3+2](Li3)F12 (M = Al, Cr, and Fe) from aqueous solution and their properties. In: *Journal of Solid State Chemistry* 20 (1977), Nr. 3, 261 - 265. http://dx.doi.org/https://doi.org/10.1016/0022-4596(77)90162-1. – DOI https://doi.org/10.1016/0022–4596(77)90162–1. – ISSN 0022–4596

[21] Massa, Bernhard P. Werner ; Babel, Dietrich: Verfeinerung der Granatstruktur des Natrium-Lithium-Eisen(III)fluorids Na3Li3Fe2F12. In: *Zeitschrift für Kristallographie - Crystalline Materials* 158 (1982), S. 299–306

[22] Novak, G. A. ; Gibbs, G. V.: The Crystal Chemistry of the Silicate Garnets. In: *American Mineralogist* 56 (1971), 06, Nr. 5-6, S. 791–825. – ISSN 0003–004X

[23] WEST, ANTHONY R. ; Edition, Student E. (Hrsg.): *Solid State Chemistry and its Applications,*. Hoboken, United States : John Wiley & Sons, Ltd, 2014. – ISBN 1119942942

[24] Barbara L Dutrow, Christine M. Clark Eastern Michigan U. Louisiana State University U. Louisiana State University: *X-ray Powder Diffraction (XRD)*. https://serc.carleton.edu/research_education/geochemsheets/techniques/XRD.html. Version: Dezember 2019

[25] Swapp, Susan: *Scanning Electron Microscopy (SEM)*. https://serc.carleton.edu/research_education/geochemsheets/techniques/SEM.html. Version: November 2019

[26] Richthofen, Georg F.: *Methodenbeschreibung zum REM und REM-EDX.* http://www.hdz-gruppe.de/fileadmin/hdz/downloads/pa/Grundlagen%20-%20Methodenbeschreibung%20REM%20und%20REM-EDX.pdf. Version: November 2019

[27] Pauly, H: Cryolite, chiolite and cryolithionite: optical data redetermined. In: *Bull. geol. Soc. Denmark* 26 (1977), November, S. 95–101

[28] Martin Philipp, BSc M.: *Ionic and Electronic Conduction in Oxides, Fluorides, and Hydrides for Li-Based Batteries*, TU Graz, Diss., 2020

[29] Langley, Richard H. ; Sturgeon, George D.: Lattice parameters and ionic radii of the oxide and fluoride garnets. In: *Journal of Solid State Chemistry* 30 (1979), Nr. 1, 79 - 82. http://dx.doi.org/https://doi.org/10.1016/0022-4596(79)90132-4. – DOI https://doi.org/10.1016/0022–4596(79)90132–4. – ISSN 0022–4596

A. Appendix

Table 6.: Used Chemicals

Chemical	CAS-Number
NaF	7681-49-4
LiF	7789-24-4
AlF_3	7783-18-1
InF_3	7783-52-0
GaF_3	7783-51-9
TiF_3	13470-08-1
CrF_3	7788-97-8
VF_3	10049-12-4
MnF_3	7783-53-1
CoF_3	10026-18-3
FeF_3	7783-50-8
MgF_2	7783-40-6
NiF_2	10028-18-9
CaF_2	7789-75-5
CuF_2	7783-19-7
ZnF_2	7783-49-5

Table 7.: Weight of Chemicals 17.4.2018

Garnet	NaF/mg	LiF/mg	MF_3/mg
NAlL	339.67	200.22	451.92
NGaL	275.34	170.97	554.23
NVL	299.94	184.24	513.40
NTiL	305.95	188.84	513.73
NMnL	294.95	183.74	524.52
NCoL	290.94	179.07	532.87
NInL	231.29	142.45	628.93

Table 8.: Weight of Chemicals 23.4.2018

Garnet	NaF/mg	LiF/mg	$MF_3(MF_2)/mg$
NCrL	301.90	185.92	517.89
NFeL	294.45	181.87	525.24
NNiL	387.62	239.17	443.43

Table 9.: Weight of Chemicals 14.5.2018 with 10% more LiF

Garnet	NML/mg	LiF/mg
NAlL	142.97	2.71
NNiL	143.65	3.61
NNiL	133.17	2.70
NNiL	134.41	2.62
NNiL	133.84	2.59

Table 10.: Weight of Chemicals 05.06.2018

Garnet	NaF/mg	LiF/mg	AlF_3/mg	NF_2/mg
NAlCaL	338.40	208.15	428.30	20.60
NAlMgL	337.40	209.70	430.42	17.16

Table 11.: Weight of Chemicals 23.7.2018

Garnet	NaF/mg	LiF/mg	$MF_3(MF_2)/mg$
NVL	838.60	510.60	1435.79
NCrL	589.00	364.57	1037.04
NCuL	1888.0	1166.30	2282.60
NMnL	2950.53	1820.08	5234.18
NCoL	2892.27	1780.96	5321.72
NZnL	2307.33	1157.73	2304.15
NTiL	3058.40	1854.57	5146.00
NNiL	1932.11	1193.25	2222.30

Table 12.: Weight of Chemicals 17.10.2018

Garnet	NaF/mg	LiF/mg	MF_3/mg
NInL	691.94	426.59	1885.27
NCrL	1018.03	627.61	1356.23

Table 13.: Weight of Chemicals 06.11.2018

Garnet	NaF/mg	LiF/mg	MF_3/mg
NCrL	1121.32	694.47	1941.39

Table 14.: Weight of Chemicals 07.11.2018

Garnet	NaF/mg	LiF/mg	MF_3/mg
NAlL	1356.12	837.21	1807.15
NInL	596.30	369.98	1628.37

Table 15.: Weight of Chemicals 08.11.2018

Garnet	NaF/mg	LiF/mg	MF_3/mg
NGaL	550.42	340.90	1109.06

Table 16.: Weight of Chemicals 15.11.2018

Garnet	NaF/mg	LiF/mg	AlF_3/mg	NF_2/mg
NAlCaL	1012.85	625.50	1282.60	64.01
NAlMgL	1014.04	628.80	1289.16	50.81

Table 17.: Weight of Chemicals 19.11.2018

Garnet	NaF/mg	LiF/mg	MF_3/mg	NF_2/mg
NGaCaL	830.83	513.76	1590.55	65.00
NGaMgL	834.74	517.47	1597.20	28.40
NInCaL	582.84	360.37	1512.60	46.40
NInMgL	585.93	363.31	1515.93	18.00

Table 18.: Weight of Chemicals 30.11.2018

Garnet	NaF/mg	LiF/mg	MF_3/mg
NVL	1050.72	648.97	1799.27
NVL	1025.76	633.00	1837.82

Table 19.: Weight of Chemicals 14.12.2018

Garnet	NaF/mg	LiF/mg	MF_3/mg	NF_2/mg
NInMgL	585.36	372.47	1514.60	28.00
NInCaL	585.50	373.34	1517.73	24.10

Table 20.: Weight of Chemicals 17.01.2019

Garnet	NaF/mg	LiF/mg	MF_3/mg	NF_2/mg
NAlMgL	846.17	540.17	1071.87	41.85
NAlCaL	846.98	541.96	1075.42	33.70

Table 21.: Weight of Chemicals 22.01.2019

Garnet	NaF/mg	LiF/mg	NF_2/mg
NCuL	823.66	848.88	1103.99

Table 22.: Weight of Chemicals 06.03.2019

Garnet	NaF/mg	LiF/mg	MF_3/mg	NF_2/mg
NTiMgL	612.53	390.73	968.15	30.60
NTiCaL	613.80	392.30	970.60	25.35
NTiCuL	605.95	386.65	959.23	48.90

Table 23.: Weight of Chemicals 12.03.2019

Garnet	NaF/mg	LiF/mg	MF_3/mg	NF_2/mg
NInMgL	474.91	312.59	1165.98	47.42
NInCaL	476.60	315.58	1170.10	38.61
NInCuL	463.39	297.81	1202.14	37.34

Table 24.: Weight of Chemicals 14.03.2019

Garnet	NaF/mg	LiF/mg	MF_3/mg	NF_2/mg
NInCaL	485.83	330.72	1126.60	58.13

Table 25.: Weight of Chemicals 4.42019 with 10% ; 15% and 20% more LiF

Garnet	NML/mg	LiF/mg
NGaML	182.36	4.98
NGaML	232.76	3.99
NGaML	234.07	8.78

Table 26.: Weight of Chemicals 26.04.2019

Garnet	NaF/mg	LiF/mg	MF_3/mg
NCrL	748.33	463.96	1293.37

Table 27.: Weight of Chemicals 15.05.2019

Garnet	NaF/mg	LiF/mg	MF_3/mg	NF_2/mg
NInZnL	463.50	296.15	1202.70	39.10

Table 28.: Weight of Chemicals 23.05.2019

Garnet	NaF/mg	LiF/mg	MF_3/mg	NF_2/mg
NInCuL	464.20	296.70	1202.17	37.58
NInMgL	467.28	299.00	1211.59	23.86

Table 29.: Weight of Chemicals 12.06.2019

Garnet	NaF/mg	LiF/mg	MF_3/mg	NF_2/mg
NInMgL	489.30	359.20	1019.97	123.20
NInMgL	543.53	447.00	740.54	270.00
NInMgL	596.47	553.49	407.13	442.70
NInMgL	662.49	682.41		655.40
NInZnL	478.88	345.40	979.20	196.80
NInZnL	497.04	411.87	680.11	410.05
NInZnL	520.80	482.95	355.40	641.90
NInZnL	544.48	560.44		894.50